



Effect of W on the acidity and redox performance of the $\text{Cu}_{0.02}\text{Fe}_{0.2}\text{W}_a\text{TiO}_x$ ($a = 0.01, 0.02, 0.03$) catalysts for NH_3 -SCR of NO

Shibo Ma, Xiaoyu Zhao, Yushi Li, Tianrui Zhang, Fulong Yuan, Xiaoyu Niu*, Yujun Zhu*

Key Laboratory of Functional Inorganic Material Chemistry (Heilongjiang University), Ministry of Education, School of Chemistry and Materials, Heilongjiang University, Harbin 150080, PR China

ARTICLE INFO

Keywords:

NH_3 -SCR
 $\text{Cu}_{0.02}\text{Fe}_{0.2}\text{W}_a\text{TiO}_x$
 Tungsten modification
 Combined effect
In-situ DRIFTS

ABSTRACT

A series of tungsten-modified $\text{Cu}_{0.02}\text{Fe}_{0.2}\text{TiO}_x$ catalysts ($\text{Cu}_{0.02}\text{Fe}_{0.2}\text{W}_a\text{TiO}_x$; $a = 0.01, 0.02$, and 0.03) was synthesized by sol-gel method. Their catalytic activities were investigated for the selective catalytic reduction (SCR) of NO with NH_3 , in the presence/absence of 5 vol.% H_2O . The characterization techniques of XRD, BET, Raman, H_2 -TPR, NH_3 -TPD, XPS, *in situ* DRIFTS, and kinetic studies were used to reveal the effect of tungsten modification on the redox and acidity of the $\text{Cu}_{0.02}\text{Fe}_{0.2}\text{W}_a\text{TiO}_x$ catalysts. The relationship among the species composition, acid property, and oxidation-reduction behavior of the $\text{Cu}_{0.02}\text{Fe}_{0.2}\text{W}_a\text{TiO}_x$ catalysts was established. Results demonstrated that a moderate amount of tungsten doping can markedly enhance the specific surface area, improve the abundant Brönsted and Lewis acid sites, and tune the surface species composition, which all benefited high-performance catalysis. Water/sulfur resistance also improved because of the excellent acidity levels. Among the $\text{Cu}_{0.02}\text{Fe}_{0.2}\text{W}_a\text{TiO}_x$ catalysts, $\text{Cu}_{0.02}\text{Fe}_{0.2}\text{W}_{0.02}\text{TiO}_x$ showed the highest NO conversion, a wide reaction-temperature window (235–520 °C) with > 90% NO conversion, high N_2 selectivity, and high water/sulfur resistance even in the presence of 5 vol.% H_2O . Moreover, $\text{Cu}_{0.02}\text{Fe}_{0.2}\text{W}_{0.02}\text{TiO}_x$ retained its outstanding catalytic activity under a rather high gas hourly space velocity (GHSV) of 100,000 h^{-1} . In conclusion, the combined effects of redox and sufficient acidities on catalytic activity played key roles in superior SCR performance and water/sulfur durability. Furthermore, the NH_3 -SCR reaction over $\text{Cu}_{0.02}\text{Fe}_{0.2}\text{W}_{0.02}\text{TiO}_x$ may follow the Eley–Rideal reaction pathway according to the *in situ* DRIFTS and kinetic studies results.

1. Introduction

Emissions of nitrogen oxides (NO_x) from stationary sources such as fossil-fueled power plants, small- and medium-sized industrial boilers or fluidized catalytic cracking units, municipal solid-waste incineration plants, and other sources are increasing in rapidly developing countries. Thus, the abatement of these harmful pollutants is a primary goal for improving the eco-environment and protecting human health [1,2]. The selective catalytic reduction (SCR) of NO_x by NH_3 , hereafter denoted as NH_3 -SCR, in the presence of excess oxygen is an efficient and economic technique for converting NO_x into N_2 and H_2O [3–5]. $\text{V}_2\text{O}_5\text{-WO}_3(\text{MoO}_3)/\text{TiO}_2$ as traditional commercial catalysts has excellent catalytic performance but has the shortcomings of narrow reaction-temperature window (300–400 °C), biological toxicity of V, and low stability [6,7]. Thus, developing new types of NH_3 -SCR catalysts to substitute the conventional commercial catalysts is highly desirable for researchers.

In recent decades, composite metal oxides due to their advantages

of simple synthesis method, wide availability of raw materials, and low cost are widely investigated in denitrification (deNO_x) technology from stationary sources; most of these sources were transition metal oxides including FeO_x , TiO_x , CeO_x , CoO_x , NbO_x , CuO_x , and MnO_x that have been diffusely developed for the substitution of traditional V-based catalyst [1,6,8–10]. Among the various catalyst systems, iron oxides as catalytic component are environmentally benign and price moderate materials, which have the remarkable SCR activity [11–13]. Iron-titanium-based catalysts, such as FeTiO_x [14,15], $\text{Fe}_2\text{O}_3/\text{TiO}_2$ [16], $\text{Fe}_2(\text{SO}_4)_3/\text{TiO}_2$ [17], and Fe–Ti spinel ($(\text{Fe}_{3-x}\text{Ti}_x)_{1-8}\text{O}_4$) [8], have attracted considerable attention because of their outstanding medium-high temperature SCR performance. However, the operating conditions, such as the composition of flue gas and temperature (< 300 °C), of medium and small sized boilers vary greatly. Therefore, developing the deNO_x catalysts with excellent low-temperature catalytic performance, wide-working temperature window, and good water/sulfur resistance is a challenging task and has a broad application prospect.

The NH_3 -SCR performance of the iron-titanium-based catalysts can

* Corresponding authors.

E-mail addresses: niuxiaoyu@hlju.edu.cn (X. Niu), yujunzhu@hlju.edu.cn (Y. Zhu).

<https://doi.org/10.1016/j.apcatb.2019.02.015>

Received 26 July 2018; Received in revised form 1 February 2019; Accepted 9 February 2019

Available online 11 February 2019

0926-3373/ © 2019 Elsevier B.V. All rights reserved.

be significantly accelerated with doping additional components, such as ceria, manganese, copper, and tungsten. Copper was introduced to the iron-titanium catalytic system, which presented the high activity at low temperature due to its strong oxidation reduction property [18–20]. In the previous works, we reported a $\text{Cu}_{0.2}\text{-Ce}_{0.3}\text{-Zr}_{0.5}$ catalyst that exhibited remarkable $\text{NH}_3\text{-SCR}$ low-temperature activity, and the abundant acid sites were responsible for the increased activity and excellent N_2 selectivity at low temperature [21]. The $\text{Cu}_x\text{-Nb}_{1.1-x}$ bimetal oxide catalysts were also prepared by a citric acid method. The $\text{Cu}_{0.25}\text{-Nb}_{0.85}$ oxides showed a wide operating temperature window, near 100% N_2 selectivity, and high water/sulfur resistance due to the most acid amount and NO adsorption capacity [10].

Tungsten has been widely concerned and studied in traditional commercial deNO_x catalysts (V–W–Ti) [22–24], and new types of catalysts, such as iron–tungsten catalysts [2,25–27], ceria–tungsten catalysts [28,29], manganese–tungsten [30], titanium–tungsten [31], and copper–tungsten [32] have been developed in recent years. According to above studies, tungsten can lead to a prominently high dispersion and stabilization of the active phases, such as anatase TiO_2 phase, increase the surface acidity, and tune the redox capacity, enhancing the $\text{NH}_3\text{-SCR}$ activity.

Based on the above descriptions, the present work attempts to develop the novel Cu–Fe–Ti oxide catalysts with tungsten modification. Meanwhile, copper is used to improve the low-temperature activity, and the acidity and redox can be adjusted by adding tungsten to obtain the wide active temperature window. In this study, a series of $\text{Cu}_{0.02}\text{Fe}_{0.2}\text{W}_a\text{TiO}_x$ ($a = 0.01, 0.02, 0.03$) catalysts were synthesized by one-pot sol–gel method, and the modification effect of WO_x species on the $\text{NH}_3\text{-SCR}$ of NO activity over the $\text{Cu}_{0.02}\text{Fe}_{0.2}\text{W}_a\text{TiO}_x$ catalysts were investigated in detail. The contributions of the redox performance and acidity to $\text{NH}_3\text{-SCR}$ reaction were summarized according to the characterization results.

2. Experimental

2.1. Catalyst preparation

A single step sol–gel method was applied to synthesize the $\text{Cu}_{0.02}\text{Fe}_{0.2}\text{W}_a\text{TiO}_x$ ($a = 0.01, 0.02, 0.03$) oxides catalysts, where 0.02, 0.2 and a represented the molar ratio of Cu to Ti, Fe to Ti and W to Ti ($a = 0.01, 0.02, 0.03$), respectively. Briefly, ferric nitrate (0.02 mol), cupric nitrate (0.002 mol), ammonium metatungstate (0.001–0.003 mol) and water (15 mL) were mixed under vigorous stirring at room temperature for 30 min to form solution A, butyl titanate (0.1 mol) and ethanol (50 mL) were mixed to form solution B. Solution B was added dropwise into solution A with vigorous stirring for 1 h, and then acetic acid (50 mL) was added into the solution. After that, the mixture was vigorously stirred for 5 h at room temperature to form a yellow sol. The sol was transformed to gel after being stable for 5 days at room temperature. The gel was dried at 110 °C overnight and then was calcined at 500 °C for 4 h in air to obtain catalysts labeled as $\text{Cu}_{0.02}\text{Fe}_{0.2}\text{W}_a\text{TiO}_x$. In addition, $\text{Cu}_a\text{Fe}_{0.1}\text{TiO}_x$ ($a = 0.02, 0.05, 0.1$) and $\text{Cu}_{0.02}\text{Fe}_b\text{TiO}_x$ ($b = 0.1, 0.2, 0.3$) were also prepared according to the above method, in which a and b present the molar ratio of Cu to Ti and Fe to Ti, respectively.

2.2. Catalyst characterization

N_2 adsorption–desorption isotherms were measured by Micromeritics Tristar II 3020 instrument at -196 °C, and the surface area was calculated by the Brunauer–Emmett–Teller (BET) equation. Powder X-ray diffraction (XRD) measurements were carried out on a Bruker D8 Advance with Cu K α radiation (1.5418 Å) and operated at 40 kV and 40 mA, the data was recorded in a 2θ range of 10–80 ° with 0.02° intervals. The elemental mapping images of EDX measurements were recorded by FeiNa phenom pro electron microscope operating. Raman

spectroscopy was tested using a Jobin Yvon HR 800 micro-Raman spectrometer at 458 nm in the dehydrated condition. X-ray photoelectron spectroscopy (XPS) was performed on a Kratos-AXIS ULTRA DLD with Al K α X-rays. The binding energy was calibrated internally on the basis of C1s at 284.6 eV.

Temperature programmed desorption of ammonia ($\text{NH}_3\text{-TPD}$) measurements were performed on a AutoChem TP5080 chemisorption analyzer (Xianquan Tianjin, China) equipped a thermal conductivity detector (TCD). 100 mg of each catalyst was loaded in a quartz reactor and preheated at 200 °C by high purified He (30 mL min⁻¹) for 1 h and subsequently cooled down to 100 °C. After that, the catalyst was saturated with 25 mL min⁻¹ anhydrous NH_3 for 1 h at the same temperature and then flushed with He for 1 h to remove the physically absorbed NH_3 . Finally, the TPD curve was recorded from room temperature to 550 °C at the rate of 10 °C min⁻¹ in He (30 mL min⁻¹).

Temperature programmed reduction with hydrogen ($\text{H}_2\text{-TPR}$) experiments were also conducted on a AutoChem TP5080 chemisorption analyzer (Xianquan Tianjin, China) with TCD. Prior to reduction, 20 mg of the catalyst was loaded in the quartz reactor and preheated at 300 °C under pure O_2 stream (25 mL min⁻¹) for 1 h with a ramp rate of 10 °C min⁻¹. After the sample was cooled down to ambient temperature in the same stream, the catalyst was then exposed to 5% H_2/N_2 (30 mL min⁻¹), and the temperature was subsequently raised from 100 °C to 650 °C with a ramp rate of 10 °C min⁻¹.

The *in-situ* diffuse reflectance infrared Fourier transform spectra (DRIFTS) were collected on a Bruker Vector FTIR spectrometer (Nicolet 6700) with a high-sensitive MCT detector cooled by liquid N_2 and an *in situ* diffuse reflectance cell (Harrick). Prior to each test, the catalyst was heated to 310 °C for 1 h with high purified N_2 (200 cm³ min⁻¹) to remove the physically absorbed water. The background spectrum was recorded at each target temperature in N_2 atmosphere and was subtracted from the sample spectra. The spectra were measured by the parameter of 64 scans at a resolution of 4 cm⁻¹. The gas feeds used for the experiment were a mixture of 1000 ppm NH_3/N_2 , 1000 ppm NO/N_2 , 3% O_2/N_2 and 1800 ppm H_2O when used.

2.3. Catalytic activity tests

The fixed-bed quartz reactor was used for SCR activity measurement of the $\text{Cu}_{0.02}\text{Fe}_{0.2}\text{W}_a\text{TiO}_x$ catalysts in a steady state flow mode, with 0.3 mL catalyst of 40–60 meshes. Reaction conditions were as follows: 1000 ppm NH_3 , 1000 ppm NO , 3% O_2 and 5 vol.% H_2O (when used), 100 ppm SO_2 (when used), pure N_2 as the balance gas. The total flow rate of the feed gas was 200 mL min⁻¹ and gas hourly space velocity (GHSV) was of 40,000–100,000 h⁻¹. After the reaction reached stable conditions above 30 min every testing temperature, the concentrations of NO , NH_3 , NO_2 and N_2O were measured on a Nicolet 6700 FT-IR spectrometer with a gas cell (PIKE) and the concentration of NO was also measured on a chemiluminescence NO/NO_x analyzer (CLD 60). NO conversion and N_2 selectivity were calculated using the following equations:

$$\text{NO conversion (\%)} = 100\% \times ([\text{NO}]_{\text{in}} - [\text{NO}]_{\text{out}})/[\text{NO}]_{\text{in}} \quad (1)$$

$$\text{N}_2 \text{ selectivity (\%)} = 100\% \times ([\text{NO}]_{\text{in}} + [\text{NH}_3]_{\text{in}} - [\text{NO}_2]_{\text{out}} - 2[\text{N}_2\text{O}]_{\text{out}})/([\text{NO}]_{\text{in}} + [\text{NH}_3]_{\text{in}}) \quad (2)$$

Where, $[\text{NO}]_{\text{in}}$, and $[\text{NH}_3]_{\text{in}}$ refer to the inlet concentration of NO and NH_3 , respectively; $[\text{NO}]_{\text{out}}$, $[\text{NH}_3]_{\text{out}}$, $[\text{NO}_2]_{\text{out}}$ and $[\text{N}_2\text{O}]_{\text{out}}$ indicate the outlet concentration of NO , NH_3 , NO_2 and N_2O , respectively.

2.4. Kinetic measurements

Kinetic measurements were conducted on a fixed-bed quartz reactor at different temperature. The stable state and conversion of NO below 20% were accomplished in an approximate kinetic regime, the feed gas composition was as follows: 200–1000 ppm NO , 200–1000 ppm NH_3 ,

3% O₂, and N₂ in balance, GHSV was $1.0 \times 10^6 \text{ h}^{-1}$, the total flow rate was 500 mL/min, and 35 mg of catalyst (< 200 mesh size powder) was used for each run, no by-product (N₂O or NO₂) were detected in this measurements.

3. Results and discussion

3.1. Catalytic activity for NH₃-SCR

Fig. S1 in the Supplementary information (SI) shows the NH₃-SCR activity of the Cu_aFe_{0.1}TiO_x ($a = 0.02, 0.05, 0.1$) (Fig. S1 A, B) and Cu_{0.02}Fe_bTiO_x ($b = 0.1, 0.2, 0.3$) (Fig. S1C, D) catalysts. Notably, the SCR activity changed with different amounts of Cu and Fe, in which the low-temperature activity increased with the Cu content (Fig. S1 A). However, poor N₂ selectivity was obtained at high temperature with increased Cu amount (Fig. S1B). Among these catalysts, the Cu_{0.02}Fe_{0.2}TiO_x catalyst displayed high low-temperature catalytic activity with 160–350 °C, but NO conversion and N₂ selectivity decreased at > 350 °C. Moreover, weak H₂O resistance was observed for the Cu_{0.02}Fe_{0.2}TiO_x catalyst (Fig. S2 in SI). Thus, a series of tungsten-modified Cu_{0.02}Fe_{0.2}W_aTiO_x catalysts ($a = 0.01, 0.02, 0.03$) were prepared to obtain high NH₃-SCR activity with broad reaction-temperature window and high water resistance.

The catalytic performances of the Cu_{0.02}Fe_{0.2}W_aTiO_x ($a = 0, 0.01, 0.02, 0.03$) catalysts were examined in the SCR of NO with NH₃ under a gas hourly space velocity (GHSV) of 40,000 h⁻¹ (Fig. S3 in SI). The Cu_{0.02}Fe_{0.2}TiO_x catalyst showed SCR activity with the maximum NO conversion of 97.2% above 160 °C. However, the N₂ selectivity decreased significantly above 250 °C, possibly due to excessive oxidation of ammonia with increased temperature. For the Cu_{0.02}Fe_{0.2}W_aTiO_x catalysts, the activity temperature window shifted to high temperature slightly, whereas the Cu_{0.02}Fe_{0.2}W_aTiO_x catalysts exhibited excellent activity in the medium-high temperature range compared with Cu_{0.02}Fe_{0.2}TiO_x. The NO conversion reached 100% over Cu_{0.02}Fe_{0.2}W_{0.02}TiO_x at 200 °C. Remarkably, the Cu_{0.02}Fe_{0.2}W_{0.02}TiO_x catalyst showed the excellent SCR activity in the temperature range of 200–460 °C along with high N₂ selectivity beyond 95% in the whole temperature range. Therefore, tungsten addition to Cu_{0.02}Fe_{0.2}TiO_x can enhance the NO conversion and N₂ selectivity at the high temperature (> 300 °C). This phenomenon is in accordance with previous research results that existence of tungsten oxides prominently broadened the operating temperature window for NH₃-SCR reaction [27–29]. Furthermore, the increase in GHSV from 40,000 h⁻¹ to 100,000 h⁻¹ did not show an obvious influence to the SCR performance over the Cu_{0.02}Fe_{0.2}W_{0.02}TiO_x catalyst (Fig. S4 in SI). The NO conversion declined mildly at low temperature below 250 °C, whereas the high-temperature SCR activity was not visibly influenced. These results suggested that the novel Cu_{0.02}Fe_{0.2}W_{0.02}TiO_x catalyst is highly effective for NO reduction under the high-space velocity.

The NH₃-SCR reactions with 5 vol.% H₂O were also carried out as a

function of temperature over Cu_{0.02}Fe_{0.2}TiO_x and Cu_{0.02}Fe_{0.2}W_aTiO_x ($a = 0.01, 0.02, 0.03$). As shown in Fig. 1, a non-negligible inhibition effect of H₂O was observed on the NH₃-SCR performance over the four catalysts in low-temperature ranges (< 250 °C). The catalytic performance of Cu_{0.02}Fe_{0.2}TiO_x was most seriously affected by water vapor, showing the lowest NO conversion and the most narrow operating temperature window (280 °C–350 °C). Notably, the temperature of initial maximum NO conversion (95.1%) increased to 280 °C, whereas 97% of the NO conversion can be obtained at 160 °C in the absence of water. Compared with Cu_{0.02}Fe_{0.2}TiO_x, Cu_{0.02}Fe_{0.2}W_aTiO_x ($a = 0.01, 0.02, 0.03$) still exhibited the far wider activity window in the presence of water vapor (Fig. 1A). Among these Cu_{0.02}Fe_{0.2}W_aTiO_x ($a = 0.01, 0.02, 0.03$) catalysts, Cu_{0.02}Fe_{0.2}W_{0.02}TiO_x exhibited the highest NH₃-SCR performance with over 90% NO conversion in a broad temperature range of 235–520 °C. The improvement of high-temperature activity can be due to the suppression of the unselective NH₃ oxidation. The results demonstrate that the tungsten-modified Cu_{0.02}Fe_{0.2}TiO_x can obviously increase the high-temperature activity in the presence of 5 vol.% H₂O in the feeding gas. Notably, the Cu_{0.02}Fe_{0.2}W_{0.02}TiO_x catalyst still showed above 95% NO conversion in a wide temperature range from 240 °C to 470 °C under a rather high GHSV of 100,000 h⁻¹ in the presence of 5 vol.% H₂O (Fig. 1B).

3.2. Effect of SO₂ + H₂O

To explore the water vapor and SO₂ durability, 5 vol.% H₂O and 100 ppm SO₂ were individually or together added into the feed gas with GHSV of 40,000 h⁻¹ at 220 °C over the Cu_{0.02}Fe_{0.2}W_{0.02}TiO_x and Cu_{0.02}Fe_{0.2}TiO_x catalysts (Fig. 2). Before introducing SO₂ and H₂O, the SCR reaction was stabilized for approximately 2 h. Obviously, the NO removal efficiency decreased from 100% to ~53% in short time over Cu_{0.02}Fe_{0.2}TiO_x after 5% H₂O was injected into the feed gas (Fig. 2A). Further raising temperatures to 240 °C, the NO conversion increased to ~65% under the same condition. Then, 100 ppm SO₂ was added to the feed stream, and the NO conversion slightly decreased. The Cu_{0.02}Fe_{0.2}TiO_x activity was stable to approximately 100% with SO₂ steam both at 220 and 240 °C. The results demonstrate the weak H₂O resistance of Cu_{0.02}Fe_{0.2}TiO_x. However, as displayed in Fig. 2B, when 5 vol.% H₂O was injected into the feed gas for Cu_{0.02}Fe_{0.2}W_{0.02}TiO_x, the NO removal efficiency first maintained at 100% for 1 h and then slowly decreased from 100% to 82.6% within 8 h. Further raising the reaction temperature to 240 °C, the NO conversion completely recovered to 100%. Subsequently, 100 ppm SO₂ was added to the feed stream, and the NO conversion showed no decrease and maintained at least for 10 h in the sequent testing time. After that, cutting off H₂O from the feeds and the reaction operated for another 10 h, the NO conversion still remained at approximately 100%. This result suggested that whether in the presence of separate SO₂/H₂O or combined H₂O and SO₂ is not detrimental to the activity for Cu_{0.02}Fe_{0.2}W_{0.02}TiO_x at 240 °C. After cooling down to 220 °C again, the NO removal efficiency remained the

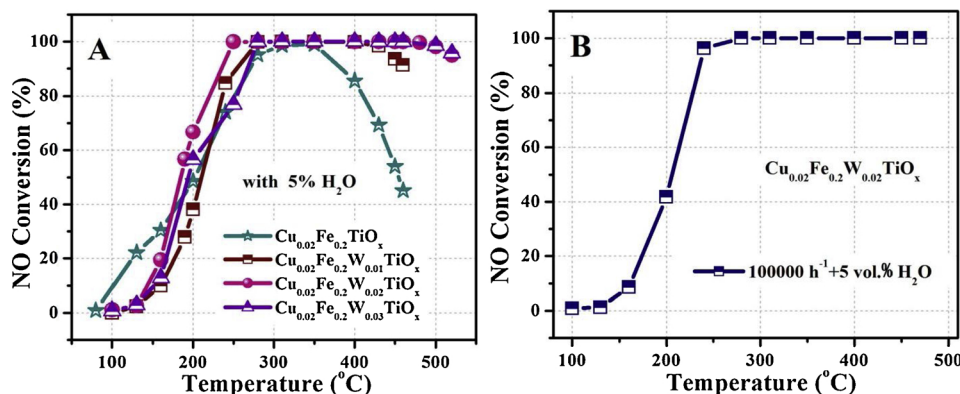


Fig. 1. NO conversion of NH₃-SCR activity over Cu_{0.02}Fe_{0.2}TiO_x and Cu_{0.02}Fe_{0.2}W_aTiO_x (A), (Reaction conditions: [NO] = [NH₃] = 1000 ppm, [O₂] = 3 vol.%, [H₂O] = 5 vol.%, N₂ as balance, GHSV = 40,000 h⁻¹). NO conversion over Cu_{0.02}Fe_{0.2}W_{0.02}TiO_x (B). (Reaction conditions: [NO] = [NH₃] = 1000 ppm, [O₂] = 3 vol.%, [H₂O] = 5 vol.%, N₂ as balance, GHSV = 100,000 h⁻¹).

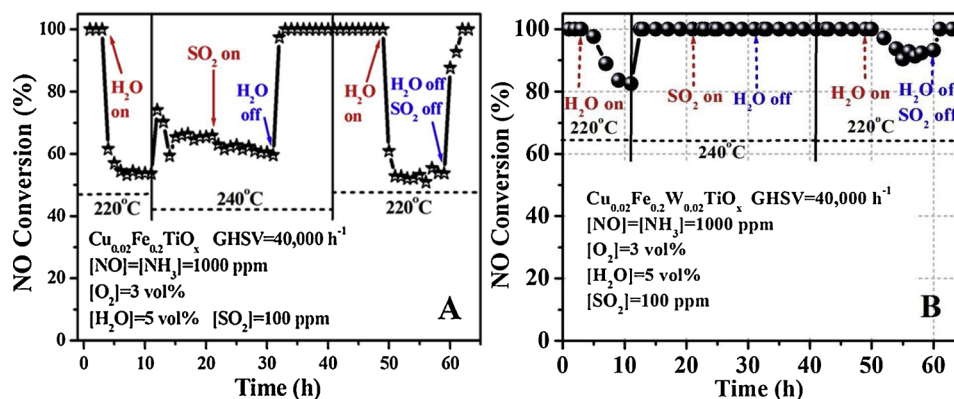


Fig. 2. Effect of SO₂, H₂O and SO₂ + H₂O on NO conversion over Cu_{0.02}Fe_{0.2}TiO_x (A) and Cu_{0.02}Fe_{0.2}W_{0.02}TiO_x (B) (Reaction conditions: [NO] = [NH₃] = 1000 ppm, [O₂] = 3 vol%, [SO₂] = 100 ppm, [H₂O] = 5 vol%, N₂ as balance, GHSV = 40,000 h⁻¹).

same after 9 h under adding 100 ppm SO₂ stream over Cu_{0.02}Fe_{0.2}W_{0.02}TiO_x. Probably, SO₂ is not harmful to Cu_{0.02}Fe_{0.2}W_{0.02}TiO_x. With adding water again, the co-existence of SO₂ and H₂O resulted slightly in decreased NO conversion (< 10%) for Cu_{0.02}Fe_{0.2}W_{0.02}TiO_x in 9 h. After switching off SO₂ and H₂O together, the NO conversion completely recovered to 100% rapidly. These results indicated that the presence of water vapor has influence on the Cu_{0.02}Fe_{0.2}W_{0.02}TiO_x activity to some extent and the effect of water vapor is reversible. Moreover, the water vapor and SO₂ durability over Cu_{0.02}Fe_{0.2}W_{0.02}TiO_x was obviously better than that over Cu_{0.02}Fe_{0.2}TiO_x, suggesting that Cu_{0.02}Fe_{0.2}W_{0.02}TiO_x catalyst had high resistance to SO₂ and H₂O steam poisoning. These results clearly revealed that Cu_{0.02}Fe_{0.2}W_{0.02}TiO_x demonstrates the satisfactory stability and durability properties, which are very significant for the practical application.

3.3. Separated NO and NH₃ oxidation

To understand in-depth the promotional effects of tungsten in the Cu_{0.02}Fe_{0.2}W_aTiO_x catalysts, the separate NO oxidation (NO + O₂) and NH₃ oxidation (NH₃ + O₂) reactions were conducted, and the results are revealed in Fig. S5 in SI. NO₂ concentration over Cu_{0.02}Fe_{0.2}W_aTiO_x was distinctly far lower than that over Cu_{0.02}Fe_{0.2}TiO_x in the whole temperature range presented in Fig. S5(A). Cu_{0.02}Fe_{0.2}W_aTiO_x showed almost no NO oxidation activity at low temperature (< 200 °C). However, more NO₂ was formed over Cu_{0.02}Fe_{0.2}W_{0.02}TiO_x than over Cu_{0.02}Fe_{0.2}W_{0.01}TiO_x and Cu_{0.02}Fe_{0.2}W_{0.03}TiO_x at above 200 °C. These results clearly demonstrated that the oxidation ability of the Cu_{0.02}Fe_{0.2}W_aTiO_x catalysts is significantly inhibited by introducing tungsten. Meanwhile, the Cu_{0.02}Fe_{0.2}W_{0.02}TiO_x catalyst has relatively higher NO oxidation capacity compared with Cu_{0.02}Fe_{0.2}W_{0.01}TiO_x and Cu_{0.02}Fe_{0.2}W_{0.03}TiO_x.

In addition, the ammonia activation and oxidation are very critical for NH₃-SCR reaction, and the relevant results of NH₃ oxidation are displayed in Fig. S5(B). For Cu_{0.02}Fe_{0.2}TiO_x, the NH₃ oxidation started at 220 °C, and approximately 50% conversion was obtained at 270 °C. The approximately total conversion (~97%) of NH₃ can be accomplished at 310 °C. By contrast, the catalysts Cu_{0.02}Fe_{0.2}W_aTiO_x displayed less than 10% NH₃ conversion at 270 °C and reached only ~64%, ~30%, and ~9% at 310 °C for Cu_{0.02}Fe_{0.2}W_{0.01}TiO_x, Cu_{0.02}Fe_{0.2}W_{0.02}TiO_x, and Cu_{0.02}Fe_{0.2}W_{0.03}TiO_x, respectively. Overall, the Cu_{0.02}Fe_{0.2}W_aTiO_x catalysts exhibit much lower ammonia conversion than Cu_{0.02}Fe_{0.2}TiO_x below 400 °C. This finding was consistent with the results of NO oxidation.

As shown in Fig. S6 in SI, the N₂ selectivity in the SCR reaction in Fig. S3B decreased with increased NH₃ conversion at above 250 °C over the Cu_{0.02}Fe_{0.2}W_aTiO_x catalysts. However, W addition can effectively improve the N₂ selectivity. For Cu_{0.02}Fe_{0.2}TiO_x, the N₂ selectivity declined

from 98.6% to 84.8% (250–450 °C), but the N₂ selectivity decreased slightly over the Cu_{0.02}Fe_{0.2}W_aTiO_x catalysts at the high temperature (> 350 °C) above 90% in the entire temperature range. Moreover, less by-products (NO₂ and N₂O) were detected. Considering the results of NH₃ oxidation, the catalytic activities for NH₃ oxidation decreased in the following order: Cu_{0.02}Fe_{0.2}TiO_x (a) > Cu_{0.02}Fe_{0.2}W_{0.01}TiO_x (b) > Cu_{0.02}Fe_{0.2}W_{0.02}TiO_x (c) > Cu_{0.02}Fe_{0.2}W_{0.03}TiO_x (d), indicating that NH₃ oxidation over the Cu_{0.02}Fe_{0.2}W_aTiO_x catalysts can be restrained effectively by adding W at elevated temperature. This modification can effectively inhibit the NH₃ over-oxidation and improve the N₂ selectivity in NH₃-SCR reaction in the high-temperature region [33].

3.4. XRD and BET surface area

To survey the essential reason for the improvement on SCR performance, analyzing their microstructure and crystallite of the Cu_{0.02}Fe_{0.2}TiO_x and Cu_{0.02}Fe_{0.2}W_aTiO_x catalysts is necessary [34]. As depicted in Fig. 3, the XRD patterns of the Cu_{0.02}Fe_{0.2}W_aTiO_x (a = 0, 0.01, 0.02, 0.03) catalysts revealed that all the samples mainly consisted of the anatase TiO₂ phase (PDF#21-1272). No evidence was observed for the formation of CuO_x and FeO_x species over the Cu_{0.02}Fe_{0.2}TiO_x and Cu_{0.02}Fe_{0.2}W_aTiO_x catalysts. This result suggested that the CuO_x and FeO_x species may be an amorphous phase or highly dispersed in the Cu_{0.02}Fe_{0.2}W_aTiO_x catalysts. Notably, no feature of crystalline tungsten oxide was also detected in low content of tungsten for Cu_{0.02}Fe_{0.2}W_{0.01}TiO_x and Cu_{0.02}Fe_{0.2}W_{0.02}TiO_x. With further increased tungsten content, some new weak diffraction peaks located at 2θ of 23.1°, 23.6°, 33.3°, and 34.2° were observed, which were ascribed

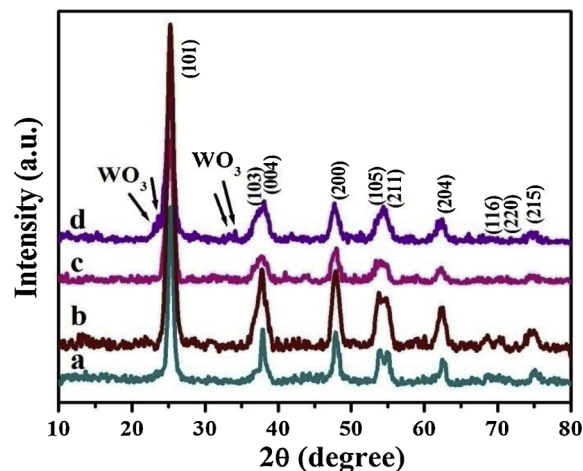


Fig. 3. XRD patterns of Cu_{0.02}Fe_{0.2}TiO_x (a), Cu_{0.02}Fe_{0.2}W_{0.01}TiO_x (b), Cu_{0.02}Fe_{0.2}W_{0.02}TiO_x (c) and Cu_{0.02}Fe_{0.2}W_{0.03}TiO_x (d).

Table 1
Textural properties, results of H₂-TPR and total acidity for different catalysts.

Catalyst	Surface area (m ² /g) ^a	Particle size (nm) ^a	Peak I + II Practical H ₂ consumption (μmol/g) ^b	CuO → Cu Theoretical H ₂ consumption (μmol/g)	Fe ₂ O ₃ → Fe ₃ O ₄ Theoretical H ₂ consumption (μmol/g)	Surface active oxygen (μmol/g) ^b	Total acidity (μmol/g) ^c
Cu _{0.02} Fe _{0.2} TiO _x	99	12.1	827	229	353	246	48.2
Cu _{0.02} Fe _{0.2} W _{0.01} TiO _x	119	8.7	666	179	280	207	67.0
Cu _{0.02} Fe _{0.2} W _{0.02} TiO _x	139	7.6	564	141	228	194	102.7
Cu _{0.02} Fe _{0.2} W _{0.03} TiO _x	127	7.7	513	125	201	187	91.2

^a BET surface area.

^b data calculate from H₂-TPR first two peaks.

^c data calculated from NH₃-TPD.

to the WO₃ crystallites (PDF#43-1035) for Cu_{0.02}Fe_{0.2}W_{0.03}TiO_x. The average crystal sizes of Cu_{0.02}Fe_{0.2}TiO_x and Cu_{0.02}Fe_{0.2}W_{0.01}TiO_x were estimated by the diffraction peak (101) based on the Scherrer formula. Cu_{0.02}Fe_{0.2}TiO_x had the largest particle size with approximately 12.1 nm, and the average particle sizes decreased after adding tungsten. Meanwhile, Cu_{0.02}Fe_{0.2}W_{0.02}TiO_x displayed the minimum particle size (approximately 7.6 nm). The XRD results apparently revealed that tungsten introduction can inhibit the nanoparticle agglomeration to a certain extent, probably leading to a high dispersion of active species.

BET surface areas of various catalysts are shown in Table 1. After introducing tungsten, the BET surface area of Cu_{0.02}Fe_{0.2}W_{0.01}TiO_x increased compared with Cu_{0.02}Fe_{0.2}TiO_x catalyst (99 m²/g) and deceased with further increased tungsten content for the Cu_{0.02}Fe_{0.2}W_{0.03}TiO_x sample. Among all catalysts, the Cu_{0.02}Fe_{0.2}W_{0.02}TiO_x catalyst exhibited the largest BET surface area (139 m²/g), attributed to the minimum particle size from the XRD results. The relative high-surface area may explain the high activity.

In addition, the SEM images and EDS elemental mapping of the Cu_{0.02}Fe_{0.2}TiO_x and Cu_{0.02}Fe_{0.2}W_{0.02}TiO_x catalysts were also performed. The corresponding results are shown in Fig. S7(A)–(I) in SI. The distributions of each element over Cu_{0.02}Fe_{0.2}TiO_x and Cu_{0.02}Fe_{0.2}W_{0.02}TiO_x are uniform, favorable to the synergistic effects between the active species and beneficial to the catalytic performance.

3.5. Raman spectroscopy analysis

Raman spectroscopy was applied to further investigate the microstructure of these synthesized samples. As shown in Fig. S8 in SI, four major peaks at 141, 385, 494, and 604 cm⁻¹ were observed and belonged to four fundamental Raman active modes of E_g (1), B_{1g}, A_{1g} + B_{1g} (2), and E_g (2) of the anatase TiO₂ structure, which was as the principal phase in all the synthesized catalysts. The weak peak located at 261 cm⁻¹ can be assigned to Fe₂O₃ phase, and the Raman peaks of Fe₂O₃ may have also overlapped at 389 and 604 cm⁻¹ [35]. The modes of E_g (2) of Cu_{0.02}Fe_{0.2}W_{0.01}TiO_x shifted slightly to higher wavenumber (blue shift) compared with Cu_{0.02}Fe_{0.2}TiO_x, which can be viewed to be the result from the creation of oxygen vacancies [12,36]. The Raman peaks of B_{1g}, A_{1g} + B_{1g} (2), and E_g (2) exhibited a red shift compared with standard TiO₂ of active modes [37], indicating that Ti–O bond length increased after the introduction of Fe³⁺, Cu²⁺ to form the Fe–O–Ti or Cu–O–Ti bond [38]. These results suggested that the metallic ions are possibly incorporated into the TiO₂ lattice combined with the XRD results [39]. Notably, an extremely broad and weak peak occurred at approximately 800, 854, and 858 cm⁻¹ for the different Cu_{0.02}Fe_{0.2}W_{0.01}TiO_x catalysts, ascribed to the vibration of crystalline WO₃ [40]. With increased tungsten content, the Raman peaks of crystalline WO₃ shifted to a low wave number (red shift), suggesting strong interactions among Ti, Fe, Cu, and W species. For Cu_{0.02}Fe_{0.2}W_{0.03}TiO_x, excess tungsten oxides may have migrated and accumulated on the TiO₂ surface to form the aggregation of the tungsten oxide species sequentially, leading to the peak shift to low wave number (800 cm⁻¹). From

the Raman results, the bands are ascribed to the tungsten species that are weak for Cu_{0.02}Fe_{0.2}W_{0.01}TiO_x and Cu_{0.02}Fe_{0.2}W_{0.02}TiO_x. Moreover, the relevant XRD patterns do not reveal any diffraction peaks belonging to crystalline WO₃. This observation suggested that the dominant WO₃ over the two catalysts are in small grain size.

3.6. H₂-TPR measurement

As presented in Fig. 4, H₂-TPR profiles of Cu_{0.02}Fe_{0.2}TiO_x and Cu_{0.02}Fe_{0.2}W_{0.01}TiO_x were measured to investigate the influence of W addition on the reducibility of the catalysts. The Cu_{0.02}Fe_{0.2}TiO_x catalyst displayed four reduction peaks at 199, 242, 489, and 662 °C. According to the literature [41], the reduction peak (I) at 199 °C was assigned to the highly dispersed surface CuO clusters, and the peak (II) at 242 °C was ascribed to the reduction of polymerized CuO, Fe₂O₃ to Fe₃O₄ and the surface active oxygen species. The subsequent two reduction peaks at the relative high temperature may be attributed to the reduction of Fe₃O₄ to FeO (489 °C) and FeO to Fe (662 °C) [42]. By contrast, after introducing different amounts of tungsten, the H₂-TPR profiles for the Cu_{0.02}Fe_{0.2}W_{0.01}TiO_x catalysts also exhibited four reduction peaks except Cu_{0.02}Fe_{0.2}W_{0.01}TiO_x. However, the reduction temperature of all the peaks shifted considerably toward the high value with increased W content. Moreover, the order of the reduction temperature for each peak was Cu_{0.02}Fe_{0.2}TiO_x < Cu_{0.02}Fe_{0.2}W_{0.01}TiO_x < Cu_{0.02}Fe_{0.2}W_{0.02}TiO_x < Cu_{0.02}Fe_{0.2}W_{0.03}TiO_x, suggesting that the reducibility of the Cu_{0.02}Fe_{0.2}W_{0.01}TiO_x catalysts were restrained compared with Cu_{0.02}Fe_{0.2}TiO_x catalyst. This result may be due to the fact that the tungsten species polymerizes or covers on the surface and the reduction of the Cu and Fe oxides can be limited by tungsten oxide. Therefore, the Cu_{0.02}Fe_{0.2}TiO_x catalyst has much stronger redox ability than the Cu_{0.02}Fe_{0.2}W_{0.01}TiO_x catalysts. This result was also in accordance with the

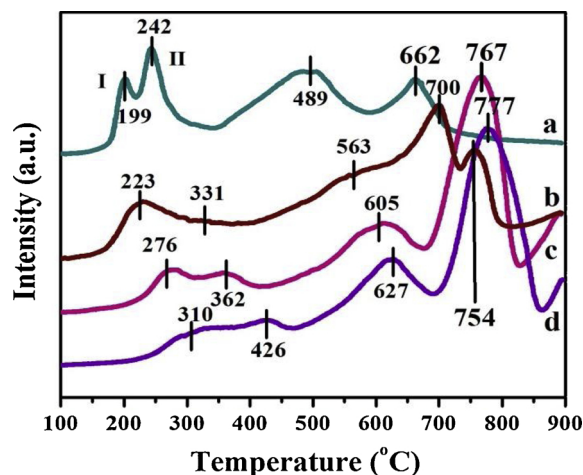


Fig. 4. H₂-TPR profiles of Cu_{0.02}Fe_{0.2}TiO_x (a), Cu_{0.02}Fe_{0.2}W_{0.01}TiO_x (b), Cu_{0.02}Fe_{0.2}W_{0.02}TiO_x (c), and Cu_{0.02}Fe_{0.2}W_{0.03}TiO_x (d).

high low-temperature activity of $\text{Cu}_{0.02}\text{Fe}_{0.2}\text{TiO}_x$.

Furthermore, the H_2 consumption corresponding to peak I + II were calculated, and the values are listed in Table 1. The practical H_2 consumption of peak I + II increased in the following order: $\text{Cu}_{0.02}\text{Fe}_{0.2}\text{W}_{0.03}\text{TiO}_x < \text{Cu}_{0.02}\text{Fe}_{0.2}\text{W}_{0.02}\text{TiO}_x < \text{Cu}_{0.02}\text{Fe}_{0.2}\text{W}_{0.01}\text{TiO}_x < \text{Cu}_{0.02}\text{Fe}_{0.2}\text{TiO}_x$. The H_2 consumption decreased with increased tungsten content possibly due to the decrease in copper and iron contents in unit mass in the $\text{Cu}_{0.02}\text{Fe}_{0.2}\text{W}_a\text{TiO}_x$ catalysts after tungsten addition. Additionally, the results in Table 1 showed that the surface-active oxygen over the $\text{Cu}_{0.02}\text{Fe}_{0.2}\text{W}_a\text{TiO}_x$ catalysts gradually decreased with increased tungsten.

The third hydrogen reduction peak can arise partially from Fe_3O_4 to FeO for the $\text{Cu}_{0.02}\text{Fe}_{0.2}\text{W}_a\text{TiO}_x$ catalysts, and the peak area increased with increased tungsten amount. This phenomenon demonstrates that the extra peak area can be attributable to the reduction of octahedral coordinated tungsten oxide species ($\text{W}^{6+} \rightarrow \text{W}^{5+} \rightarrow \text{W}^{4+}$) [43,44]. A distinct and large area peak occurred at high temperature between 650 and 900 °C, which can correspond to the reduction of subsurface amorphous tetrahedral tungsten oxide species [43,44]. According to literature [43,44], the reduction peaks in the range of 400 °C to 600 °C can be ascribed to the reduction of octahedral coordinated tungsten oxide species. Horsley et al. [43] reported that tetrahedral tungsten oxide species are extremely difficult to be reduced at concentrations below the monolayer because of a strong interaction between the isolate and dimeric state tungsten species and support. With further increased tungsten content, the superabundant tungsten species would transform into octahedral structure from tetrahedral structure, and the reducibility becomes easy [43,45]. In general, W addition reduces the redox ability of the $\text{Cu}_{0.02}\text{Fe}_{0.2}\text{W}_a\text{TiO}_x$ catalysts, which is favorable for the N_2 selectivity at high-reaction temperature. The above results indicate strong interactions among the copper, iron, and tungsten oxides in $\text{Cu}_{0.02}\text{Fe}_{0.2}\text{W}_a\text{TiO}_x$, influencing their reducibility derived from tungsten addition.

To further study the effect of tungsten on the redox properties of iron and copper oxides in the $\text{Cu}_{0.02}\text{Fe}_{0.2}\text{W}_a\text{TiO}_x$ catalysts, the reducibility of $\text{Fe}_{0.2}\text{W}_{0.02}\text{TiO}_x$, $\text{Cu}_{0.02}\text{W}_{0.02}\text{TiO}_x$, $\text{Cu}_{0.02}\text{Fe}_{0.2}\text{W}_{0.02}\text{TiO}_x$, $\text{Cu}_{0.02}\text{Fe}_{0.2}\text{TiO}_x$, $\text{Fe}_{0.1}\text{TiO}_x$, and $\text{Cu}_{0.1}\text{TiO}_x$ was also investigated by H_2 -TPR experiments. As shown in Fig. S9 in SI, the H_2 -TPR profile of $\text{Cu}_{0.1}\text{TiO}_x$ exhibited two reduction peaks at 142 and 196 °C, corresponding to the reduction of the highly dispersed surface CuO and polymerized CuO , respectively (Fig. S9a). For $\text{Cu}_{0.02}\text{W}_{0.02}\text{TiO}_x$ (Fig. S9e), the first reduction peak of copper oxides mainly occurs at 418 °C and delayed at approximately 276 °C compared with $\text{Cu}_{0.1}\text{TiO}_x$. The same situation occurred to the $\text{Fe}_{0.2}\text{W}_{0.02}\text{TiO}_x$ sample (Fig. S9f). The $\text{Fe}_2\text{O}_3 \rightarrow \text{Fe}_3\text{O}_4 \rightarrow \text{FeO} \rightarrow \text{Fe}$ reduction occurred at much higher temperature compared with $\text{Fe}_{0.1}\text{TiO}_x$ (Fig. S9b). These results indicated that tungsten introduction can strongly restrain the reduction of Fe and Cu oxides in $\text{Fe}_{0.2}\text{W}_{0.02}\text{TiO}_x$ and $\text{Cu}_{0.02}\text{W}_{0.02}\text{TiO}_x$, respectively.

However, compared with $\text{Fe}_{0.2}\text{W}_{0.02}\text{TiO}_x$ and $\text{Cu}_{0.02}\text{W}_{0.02}\text{TiO}_x$, all reduction peaks of Fe, Cu, and W oxide species in $\text{Cu}_{0.02}\text{Fe}_{0.2}\text{W}_{0.02}\text{TiO}_x$ appeared at low temperature (Fig. S9d), indicating that the $\text{Cu}_{0.02}\text{Fe}_{0.2}\text{W}_{0.02}\text{TiO}_x$ has better reducibility than $\text{Fe}_{0.2}\text{W}_{0.02}\text{TiO}_x$ and $\text{Cu}_{0.02}\text{W}_{0.02}\text{TiO}_x$. This result can reflect the strong interaction among Cu, Fe, and W oxides, possibly forming Cu–O–Fe, Cu–O–W, and Fe–O–W structures in the $\text{Cu}_{0.02}\text{Fe}_{0.2}\text{W}_a\text{TiO}_x$ catalysts [2,26,32]. This condition can enhance the oxidation capacity of the Cu and Fe oxide species. The reduction peaks of tungsten oxides also occurred at low temperature, suggesting that the strong interaction can also be an efficient promoter to the tungsten oxide reducibility.

In addition, regarding the H_2 -TPR curves of the $\text{Cu}_{0.02}\text{Fe}_{0.2}\text{TiO}_x$, $\text{Fe}_{0.1}\text{TiO}_x$, and $\text{Cu}_{0.1}\text{TiO}_x$ samples, the redox property of the Fe oxide species in $\text{Cu}_{0.02}\text{Fe}_{0.2}\text{TiO}_x$ was obviously promoted (Fig. S9c). On the contrary, the oxidation capacity of Cu oxide species was delayed in $\text{Cu}_{0.02}\text{Fe}_{0.2}\text{TiO}_x$. The results also confirmed that the interaction between copper and iron oxides exists in $\text{Cu}_{0.02}\text{Fe}_{0.2}\text{TiO}_x$.

In conclusion, although tungsten introduction can inhibit the redox

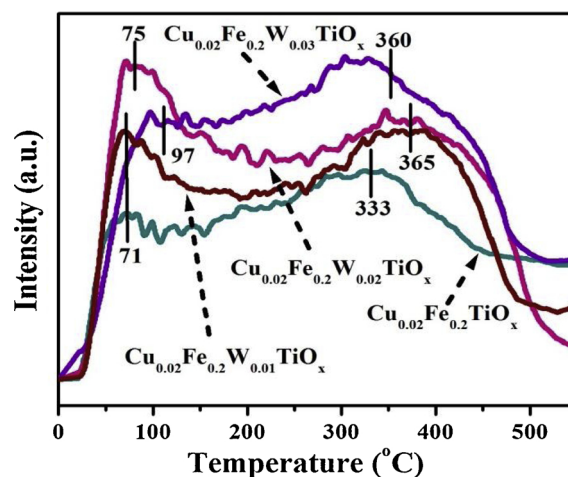


Fig. 5. NH_3 -TPD curves of $\text{Cu}_{0.02}\text{Fe}_{0.2}\text{TiO}_x$ and $\text{Cu}_{0.02}\text{Fe}_{0.2}\text{W}_a\text{TiO}_x$.

property of CuO_x and FeO_x in $\text{Cu}_{0.02}\text{W}_{0.02}\text{TiO}_x$ and $\text{Fe}_{0.2}\text{W}_{0.02}\text{TiO}_x$, respectively, the redox capacity of the $\text{Cu}_{0.02}\text{Fe}_{0.2}\text{W}_{0.02}\text{TiO}_x$ catalyst is clearly enhanced compared with $\text{Cu}_{0.02}\text{W}_{0.02}\text{TiO}_x$ and $\text{Fe}_{0.2}\text{W}_{0.02}\text{TiO}_x$. This finding suggests the strong interaction among copper, iron, and tungsten oxides in $\text{Cu}_{0.02}\text{Fe}_{0.2}\text{W}_{0.02}\text{TiO}_x$.

3.7. NH_3 -TPD analysis

The surface acidity of a catalyst is another critical factor for the NH_3 -SCR. To investigate the impact of introducing tungsten on the acid properties, NH_3 -TPD was performed to compare the acidity on the four samples. As shown in Fig. 5, all the catalysts exhibited two large ammonia desorption peaks. The desorption peak below 200 °C can be attributed to the ammonia desorbed from weakly acid sites, whereas the peak between 200 and 550 °C can be assigned to the moderately strong acid sites [46]. Apparently, the ammonia desorption peak areas of the $\text{Cu}_{0.02}\text{Fe}_{0.2}\text{TiO}_x$ catalyst at both 71 and 333 °C were smaller than those of the $\text{Cu}_{0.02}\text{Fe}_{0.2}\text{W}_a\text{TiO}_x$ catalysts. The acid amount was calculated based on desorption peak area and displayed in Table 1. The sequence of the acid amount is as follows: $\text{Cu}_{0.02}\text{Fe}_{0.2}\text{W}_{0.02}\text{TiO}_x$ (102.7 $\mu\text{mol/g}$) > $\text{Cu}_{0.02}\text{Fe}_{0.2}\text{W}_{0.03}\text{TiO}_x$ (91.2 $\mu\text{mol/g}$) > $\text{Cu}_{0.02}\text{Fe}_{0.2}\text{W}_{0.01}\text{TiO}_x$ (67.0 $\mu\text{mol/g}$) > $\text{Cu}_{0.02}\text{Fe}_{0.2}\text{TiO}_x$ (48.2 $\mu\text{mol/g}$). Meanwhile, the $\text{Cu}_{0.02}\text{Fe}_{0.2}\text{W}_{0.02}\text{TiO}_x$ catalyst possessed the maximum acid amount among the $\text{Cu}_{0.02}\text{Fe}_{0.2}\text{W}_a\text{TiO}_x$ catalysts. The acid amount slightly declined with further adding tungsten, which should be related to the formation of WO_3 phase confirmed by the XRD results (Fig. 3). The above results demonstrated that the acidity can be obviously improved after tungsten addition, which may influence the NH_3 adsorption and eventually results in the special catalytic performance.

3.8. XPS analysis

XPS investigations were undertaken to identify the surface chemical compositions and oxidation states. The XPS spectra of $\text{Fe}2p$, $\text{Cu}2p$, $\text{W}4f$, $\text{Ti}2p$, and $\text{O}1s$ for the $\text{Cu}_{0.02}\text{Fe}_{0.2}\text{W}_a\text{TiO}_x$ catalysts are collected and displayed in Fig. 6. In the $\text{Fe}2p$ spectra (Fig. 6(A)), the peaks located at 711.2 eV can be referred to the $\text{Fe}2p_{3/2}$ and $\text{Fe}2p_{1/2}$ spin-orbit peaks presented by the binding energy (BE) of 725.0 eV. The $\text{Fe}2p_{3/2}$ spectra at 711.2 eV was asymmetrical at low BE and can be fitted into two characteristic peaks by performing the peak fitting deconvolution. The BE centered at 710.9 and 712.4 eV can be assigned to Fe^{2+} and Fe^{3+} , respectively [47]. After the tungsten introduction, the BE showed no obvious change in the corresponding position. This condition may have resulted from the neighboring environment of Fe species maintaining a similar chemical environment with tungsten doping. In addition, the Fe^{3+} ratio to total Fe species ($\text{Fe}^{3+} + \text{Fe}^{2+}$) ($\text{Fe}^{3+}/(\text{Fe}^{3+} + \text{Fe}^{2+})$)

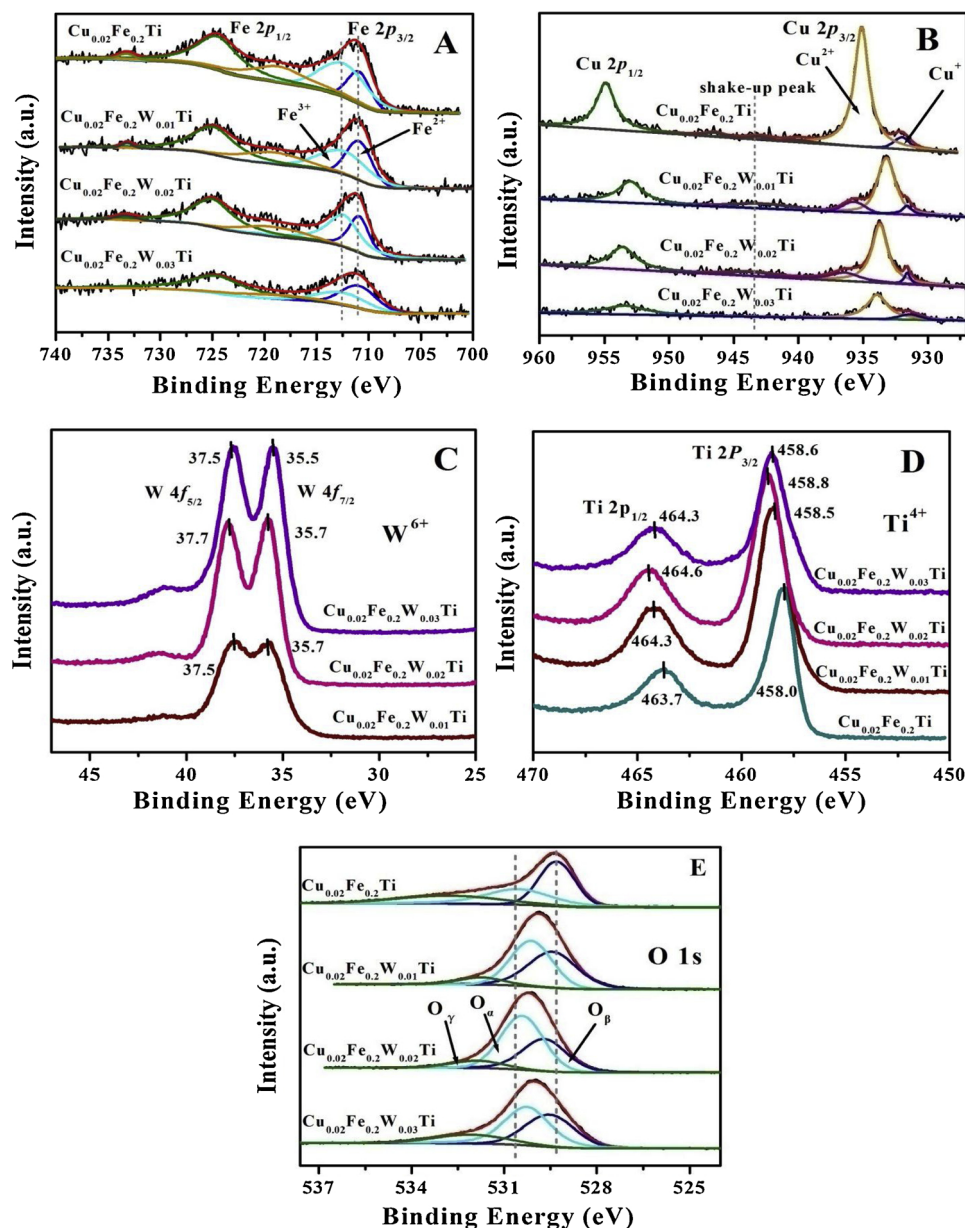


Fig. 6. XPS of Fe2p (A), Cu2p (B), W4f (C), Ti2p (D) and O1s (E) of $\text{Cu}_{0.02}\text{Fe}_{0.2}\text{TiO}_x$ and $\text{Cu}_{0.02}\text{Fe}_{0.2}\text{W}_a\text{TiO}_x$.

Table 2

Surface component of different species from XPS data over $\text{Cu}_{0.02}\text{Fe}_{0.2}\text{W}_a\text{TiO}_x$ samples.

catalyst	$\text{Fe}^{3+}/(\text{Fe}^{3+} + \text{Fe}^{2+})$	$\text{Fe}_s^{3+} \%$ ^a	$\text{Cu}^{2+}/(\text{Cu}^{2+} + \text{Cu}^+)$	$\text{O}_\alpha/(\text{O}_\alpha + \text{O}_\beta)$
$\text{Cu}_{0.02}\text{Fe}_{0.2}\text{TiO}_x$	0.68	6.53	0.92	0.39
$\text{Cu}_{0.02}\text{Fe}_{0.2}\text{W}_{0.01}\text{TiO}_x$	0.56	3.92	0.91	0.50
$\text{Cu}_{0.02}\text{Fe}_{0.2}\text{W}_{0.02}\text{TiO}_x$	0.61	3.66	0.93	0.60
$\text{Cu}_{0.02}\text{Fe}_{0.2}\text{W}_{0.03}\text{TiO}_x$	0.43	2.02	0.87	0.56

^a $\text{Fe}_s^{3+} \% = \text{Fe}_s \times [\text{Fe}^{3+}/(\text{Fe}^{3+} + \text{Fe}^{2+})]$; Fe_s : surface atomic concentrations in Table S1.

reduced after W addition (Table 2). The surface Fe^{3+} species percent (Fe_s^{3+}) was also calculated by the surface Fe atomic concentration (Table S1 in SI) times the $\text{Fe}^{3+}/(\text{Fe}^{3+} + \text{Fe}^{2+})$ ratio for these catalysts. As depicted in Table 2, the Fe_s^{3+} content on $\text{Cu}_{0.02}\text{Fe}_{0.2}\text{W}_a\text{TiO}_x$ (2.0%–3.9%) is far lower than that on $\text{Cu}_{0.02}\text{Fe}_{0.2}\text{TiO}_x$ (6.5%) and decreased from 3.9% to 2.0% for $\text{Cu}_{0.02}\text{Fe}_{0.2}\text{W}_a\text{TiO}_x$ with increased W amount. In other words, W doping resulted in decreased surface Fe^{3+} content, suggesting reduction of the redox ability of catalyst.

XPS of Cu2p in $\text{Cu}_{0.02}\text{Fe}_{0.2}\text{W}_a\text{TiO}_x$ are displayed in Fig. 6(B). Two

characteristic peaks attributed to Cu 2p_{3/2} and Cu 2p_{1/2} were observed at 927–960 eV for the four samples. A shake-up satellite peaks at ~943.0 eV and a main peak at 935.1–933.2 eV in the Cu2p_{3/2} spectra illustrate the presence of the Cu^{2+} species [48]. The weak peak at 932–931.4 eV can be ascribed to the Cu^+ species [32,49]. The peak fitting results reveal that the Cu^{2+} species mainly exists in the four samples, and the ratio of $\text{Cu}^{2+}/(\text{Cu}^{2+} + \text{Cu}^+)$ was calculated by the XPS area shown in Table 2. Notably, $\text{Cu}_{0.02}\text{Fe}_{0.2}\text{W}_a\text{TiO}_x$ presents similar $\text{Cu}^{2+}/(\text{Cu}^{2+} + \text{Cu}^+)$ ratio compared with $\text{Cu}_{0.02}\text{Fe}_{0.2}\text{TiO}_x$, indicating

the minimal influence of tungsten addition on the Cu species.

W4f spectra of the $\text{Cu}_{0.02}\text{Fe}_{0.2}\text{W}_a\text{TiO}_x$ catalysts are depicted in Fig. 6(C). The spectra of all the catalysts centered at 35.5–35.7 and 37.5–37.7 eV can be assigned to $\text{W}4f_{7/2}$ and $\text{W}4f_{5/2}$ of W (VI) oxidation state, respectively [27]. For Ti2p spectra (Fig. 6(D)), the two wide peaks of $\text{Ti}2p_{3/2}$ and $\text{Ti}2p_{1/2}$ core levels were observed at approximately 458 and 463.7 eV, presented as the chemical state of Ti^{4+} on $\text{Cu}_{0.02}\text{Fe}_{0.2}\text{TiO}_x$ [7]. Meanwhile, the Ti2p position of $\text{Cu}_{0.02}\text{Fe}_{0.2}\text{W}_a\text{TiO}_x$ shifted toward high BE after tungsten addition, indicating the existence of the strong interaction among these components combined with the above XPS results of Fe, Cu, W, and Ti.

Additionally, the O1s XPS of all catalysts are displayed in Fig. 6(E). The peak at 530.1–530.4 eV was denoted as O_a , which can be attributed to the surface-chemisorbed labile oxygen, such as O_2^- , O^- (defect-oxygen), and hydroxyl-like group (OH^-). The BE at 529.3–529.7 eV corresponded to the lattice oxygen O^{2-} from the metal oxides (denoted as O_b), and the BE above 532.0 eV was related to the adsorbed molecular water (denoted as O_c) [11,21,39]. As displayed in Table 2, the relative $\text{O}_a/(\text{O}_a + \text{O}_b)$ ratio of $\text{Cu}_{0.02}\text{Fe}_{0.2}\text{W}_a\text{TiO}_x$ was much higher than that of $\text{Cu}_{0.02}\text{Fe}_{0.2}\text{TiO}_x$. The order of the $\text{O}_a/(\text{O}_a + \text{O}_b)$ ratio was $\text{Cu}_{0.02}\text{Fe}_{0.2}\text{W}_{0.02}\text{TiO}_x$ (0.6) > $\text{Cu}_{0.02}\text{Fe}_{0.2}\text{W}_{0.03}\text{TiO}_x$ (0.56) > $\text{Cu}_{0.02}\text{Fe}_{0.2}\text{W}_{0.01}\text{TiO}_x$ (0.50) > $\text{Cu}_{0.02}\text{Fe}_{0.2}\text{TiO}_x$ (0.39), indicating that the presence of strong interaction between these element components can generate extra surface oxygen. Several surface active oxygen or surface hydroxyl species as an important source of Brønsted acid sites were generated over the $\text{Cu}_{0.02}\text{Fe}_{0.2}\text{W}_{0.02}\text{Ti}$ sample. Based on the previous research, the surface oxygen (O_a) possessed faster and more efficient electron mobility than lattice oxygen, which acted as a key role to facilitate the activation of NH_3 to form NH_2^- [14].

3.9. In situ DRIFTS

3.9.1. NH_3 adsorption ability and surface acidity

To further understand the increase in surface acidity over $\text{Cu}_{0.02}\text{Fe}_{0.2}\text{W}_a\text{TiO}_x$ induced by doping tungsten, the adsorption behavior of NH_3 on the surface of the $\text{Cu}_{0.02}\text{Fe}_{0.2}\text{W}_a\text{TiO}_x$ and $\text{Cu}_{0.02}\text{Fe}_{0.2}\text{TiO}_x$ catalysts were investigated by *in situ* DRIFTS. Before any adsorption experiments, the sample was purged with high-purity N_2 at 310 °C for 1 h and then exposed to 1000 ppm NH_3 for 30 min at 130 °C. *In situ* DRIFTS with temporal evolution was also recorded (Fig. 7(A)). Several vibration bands can be detected after NH_3 adsorbed on $\text{Cu}_{0.02}\text{Fe}_{0.2}\text{TiO}_x$ at 130 °C. A major band at 1605 cm^{-1} and two weak bands at 1238 and 1157 cm^{-1} were ascribed to the asymmetric and symmetric bending vibrations of the N–H bonds coordinated NH_3 chemisorbed on Lewis acid sites [50], and those at 3390 , 3355 , 3251 and 3152 cm^{-1} were assigned to the N–H stretching vibration modes of NH_3 adsorbed on the

Lewis acid sites [13]. Some negative bands at approximately 3628 , 3692 , and 3720 cm^{-1} were ascribed to the consumption of the surfaced hydroxyl ($-\text{OH}$) groups [51]. The only band located at 1695 cm^{-1} corresponded to the symmetric deformation modes of the NH_4^+ (δ_s (NH_4^+)) species linked to Brønsted acid sites [17,27,52].

The *in situ* DRIFTS of NH_3 adsorption over $\text{Cu}_{0.02}\text{Fe}_{0.2}\text{W}_a\text{TiO}_x$ were quite different from that of $\text{Cu}_{0.02}\text{Fe}_{0.2}\text{TiO}_x$. Abundant Brønsted acid sites were produced for the tungsten-modified $\text{Cu}_{0.02}\text{Fe}_{0.2}\text{W}_a\text{TiO}_x$ catalysts. The bands at approximately 1604 , 1257 , 1208 , 3389 , 3321 , 3251 , and 3152 cm^{-1} were associated with coordinated and the N–H stretching vibration modes of NH_3 . The bands at approximately 1735 , 1675 , and 1443 cm^{-1} corresponded to the NH_4^+ species on Brønsted acid sites [28]. In addition, the only one negative band at 3647 cm^{-1} can belong to the isolated surfaced hydroxyl ($-\text{OH}$) group. Notably, the new bands linked to NH_4^+ (1735 and 1443 cm^{-1}) on $\text{Cu}_{0.02}\text{Fe}_{0.2}\text{W}_a\text{TiO}_x$ can be attributed to the NH_3 adsorbed on the W–OH sites that arise from partially hydrated tungsten species, i.e., $\text{W}=\text{O}$ and $\text{W}-\text{O}-\text{W}$ [28,31]. Furthermore, the bands belonging to the coordinated NH_3 acid sites at ~ 1277 and $\sim 1208\text{ cm}^{-1}$ over $\text{Cu}_{0.02}\text{Fe}_{0.2}\text{W}_a\text{TiO}_x$ exhibited a red shift compared with $\text{Cu}_{0.02}\text{Fe}_{0.2}\text{TiO}_x$ (1300 cm^{-1}), and the intensity of the two bands was obviously stronger than that of $\text{Cu}_{0.02}\text{Fe}_{0.2}\text{TiO}_x$. These results demonstrated that the Lewis acid sites (~ 1277 and $\sim 1208\text{ cm}^{-1}$) over $\text{Cu}_{0.02}\text{Fe}_{0.2}\text{W}_a\text{TiO}_x$ are changed, and some of which can be corresponding to the unsaturated W^{n+} species. The adsorption behavior of NH_3 on the surface of the $\text{Cu}_{0.02}\text{Fe}_{0.2}\text{W}_a\text{TiO}_x$ and $\text{Cu}_{0.02}\text{Fe}_{0.2}\text{TiO}_x$ catalysts were also investigated by *in situ* DRIFTS at 240 °C (Fig. S10). The bands at 240 °C were almost the same as those at 130 °C. However, the peak intensity is weak. Thus, tungsten introduction results in more acid sites including both Lewis acid sites ($\text{W}=\text{O}$) and Brønsted acid sites ($\text{W}-\text{OH}$) for $\text{Cu}_{0.02}\text{Fe}_{0.2}\text{W}_a\text{TiO}_x$, and the enhanced acid sites can be beneficial to the catalytic activity.

The amount of Brønsted and Lewis acid was calculated for four catalysts based on the total acid amount from NH_3 -TPD (Fig. 5) and the ratio of peak area on each acid site from *in situ* DRIFTS (Fig. 7(A)). As displayed in Fig. 7(B), the surface of $\text{Cu}_{0.02}\text{Fe}_{0.2}\text{W}_{0.02}\text{TiO}_x$ possessed a large number of Brønsted acid sites, and the Lewis acid sites also augmented along with adding tungsten. Quite clearly, a remarkable increase in Brønsted acid sites is observed with tungsten introduction. The ratio of Brønsted acid sites (B-acid) to Lewis acid sites (L-acid) sites rose up from $\text{Cu}_{0.02}\text{Fe}_{0.2}\text{TiO}_x$, $\text{Cu}_{0.02}\text{Fe}_{0.2}\text{W}_{0.01}\text{TiO}_x$ to $\text{Cu}_{0.02}\text{Fe}_{0.2}\text{W}_{0.02}\text{TiO}_x$ and then decreased for $\text{Cu}_{0.02}\text{Fe}_{0.2}\text{W}_{0.03}\text{TiO}_x$. Thus, both Brønsted and Lewis acid sites were promoted when the appropriate content of tungsten was introduced, especially for the formation of Brønsted acid sites. The proper acidity would avail the activation of ammonia, ameliorate the high-temperature activity, and effectively inhibit the excessive

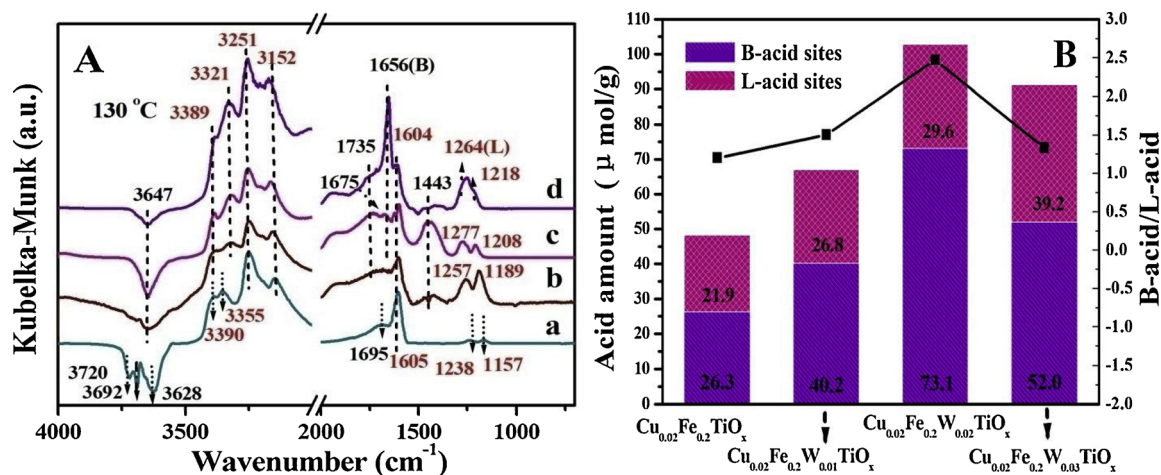


Fig. 7. *In-situ* DRIFTS of NH_3 adsorption on $\text{Cu}_{0.02}\text{Fe}_{0.2}\text{TiO}_x$ and $\text{Cu}_{0.02}\text{Fe}_{0.2}\text{W}_a\text{TiO}_x$ at 130 °C $\text{Cu}_{0.02}\text{Fe}_{0.2}\text{TiO}_x$ (a), $\text{Cu}_{0.02}\text{Fe}_{0.2}\text{W}_{0.01}\text{TiO}_x$ (b), $\text{Cu}_{0.02}\text{Fe}_{0.2}\text{W}_{0.02}\text{TiO}_x$ (c) and $\text{Cu}_{0.02}\text{Fe}_{0.2}\text{W}_{0.03}\text{TiO}_x$ (d) ($[\text{NH}_3] = 1000\text{ ppm}$, N_2 as balance) (A), Acid amount of the $\text{Cu}_{0.02}\text{Fe}_{0.2}\text{TiO}_x$ and $\text{Cu}_{0.02}\text{Fe}_{0.2}\text{W}_a\text{TiO}_x$ catalysts (B).

oxidation of ammonia on $\text{Cu}_{0.02}\text{Fe}_{0.2}\text{W}_{0.02}\text{TiO}_x$, thus facilitating the N_2 selectivity.

Based on the obvious difference in the catalytic performance of $\text{Cu}_{0.02}\text{Fe}_{0.2}\text{TiO}_x$ and $\text{Cu}_{0.02}\text{Fe}_{0.2}\text{W}_{0.02}\text{TiO}_x$ in the presence of water at low temperature, the NH_3 adsorption was measured on the surface of the $\text{Cu}_{0.02}\text{Fe}_{0.2}\text{W}_{0.02}\text{TiO}_x$ and $\text{Cu}_{0.02}\text{Fe}_{0.2}\text{TiO}_x$ catalysts with or without water, and the results are shown in Fig. S11 in SI. For the $\text{Cu}_{0.02}\text{Fe}_{0.2}\text{TiO}_x$ catalyst, the intensity of all the bands corresponding to the NH_4^+ species linked to B-acid sites and coordinated NH_3 chemisorbed on L-acid sites reduced significantly in the $\text{NH}_3 + \text{H}_2\text{O}$ mixture (Fig. S11 (a)). This condition indicated that the presence of water can inhibit the ammonia adsorption on B-acid and L-acid sites seriously over the $\text{Cu}_{0.02}\text{Fe}_{0.2}\text{TiO}_x$ catalyst. On the contrary, for the $\text{Cu}_{0.02}\text{Fe}_{0.2}\text{W}_{0.02}\text{TiO}_x$ catalyst, the adsorption of ammonia on B-acid and L-acid sites was unchanged obviously in the presence/absence of H_2O (Fig. S11(b)). The above results demonstrate that the H_2O addition does not influence the NH_3 adsorption over the $\text{Cu}_{0.02}\text{Fe}_{0.2}\text{W}_{0.02}\text{TiO}_x$ catalyst, probably due to the enhanced acidity derived from the W addition. However, the SCR activity decreased after adding H_2O (Fig. 1A) compared with that without H_2O (Fig. S3) at low temperature. A possible explanation is that ammonia adsorption on the catalyst surface may not be the rate-determining step, and the NO_x reaction with adsorbed ammonia should be influenced by water that is a key step in the SCR reaction as reported in literature [53,54].

3.9.2. $\text{NO} + \text{O}_2$ adsorption

The *in situ* DRIFTS of $\text{NO} + \text{O}_2$ adsorption capacity over $\text{Cu}_{0.02}\text{Fe}_{0.2}\text{TiO}_x$ and $\text{Cu}_{0.02}\text{Fe}_{0.2}\text{W}_{0.02}\text{TiO}_x$ at 130°C are presented in Fig. S12 in SI. Various adsorbed NO_x species quickly formed over $\text{Cu}_{0.02}\text{Fe}_{0.2}\text{TiO}_x$ (Fig. S12(A)), including bridging monodentate nitrates or adsorbed NO_2 molecules (1606 cm^{-1}) [17,26], chelating bidentate nitrates (1584 and 1284 cm^{-1}) [55], monodentate nitrate species (1541 cm^{-1}), and bridging nitrates (1245 cm^{-1}) [56]. In comparison with $\text{Cu}_{0.02}\text{Fe}_{0.2}\text{TiO}_x$, a large amount of gaseous NO molecules (weakly adsorbed NO) (1895 cm^{-1}) can be observed on the $\text{Cu}_{0.02}\text{Fe}_{0.2}\text{W}_{0.02}\text{TiO}_x$ catalyst [39]. Weak bridging bidentate nitrates or gas-phase NO_2 (1624 cm^{-1}) [42,57], bridging monodentate nitrates (1599 cm^{-1}), and chelating bidentate nitrates (1575 cm^{-1}) were also detected. Other adsorbed NO_x species cannot be found on the surface of the $\text{Cu}_{0.02}\text{Fe}_{0.2}\text{W}_{0.02}\text{TiO}_x$ catalyst (Fig. S12(B)). The comparison results show that the $\text{Cu}_{0.02}\text{Fe}_{0.2}\text{W}_{0.02}\text{TiO}_x$ catalyst has much weak adsorption capacity of NO_x , attributed to tungsten addition.

3.9.3. Reaction between NO_x and NH_3 species

The reactivity of surface NO_x and NH_3 species was also studied at 130°C (Fig. 8). As presented in Fig. 8(A), the $\text{Cu}_{0.02}\text{Fe}_{0.2}\text{TiO}_x$ catalyst was covered by several adsorbed NH_3 species (1695 , 1605 , 1238 , and 1157 cm^{-1}) after pre-adsorption with ammonia at 130°C . Followed by switching the $\text{NO} + \text{O}_2$ into the cell (after N_2 purged), monodentate nitrate species (1538 cm^{-1}) occurred immediately, the coordinated NH_3 diminished within 10 min, and NH_4^+ species vanished after approximately 5 min, which were substituted by different surface nitrate species. The above results demonstrated that all the adsorbed NH_3 species can participate in NH_3 -SCR reaction over the $\text{Cu}_{0.02}\text{Fe}_{0.2}\text{TiO}_x$ catalyst.

For $\text{Cu}_{0.02}\text{Fe}_{0.2}\text{W}_{0.02}\text{TiO}_x$ (Fig. 8(B)), several adsorbed NH_3 species were detected at the corresponding locations after the pretreatment with NH_3 at 130°C as mentioned above in Fig. 7(A). Additionally, those surface NH_3 adsorption species on $\text{Cu}_{0.02}\text{Fe}_{0.2}\text{W}_{0.02}\text{TiO}_x$ were much more reactive because all the bands of the adsorbed NH_3 disappeared between 2 and 5 min after $\text{NO} + \text{O}_2$ introduction at 130°C . This result indicated that the surfaces coordinated NH_3 and NH_4^+ species can react simultaneously with $\text{NO} + \text{O}_2$ and are consumed at a high-reaction rate. Therefore, combined with the NO_x adsorption results (Fig. S12(B)), based on the effective reaction between pre-adsorbed NH_3 species and NO , as hypothesized, the NH_3 -SCR reaction may probably

follow the Eley–Rideal (E–R) pathway over $\text{Cu}_{0.02}\text{Fe}_{0.2}\text{W}_{0.02}\text{TiO}_x$. All of the adsorbed NH_3 species exhibit a rapid consumption at elevated temperatures (Fig. S13 in SI), and the *in situ* DRIFTS results at high (240°C) and low (130°C) temperatures are consistent.

The NO_x reactivity and the surface pre-adsorbed $\text{NH}_3 + \text{H}_2\text{O}$ were also studied at 130°C over the $\text{Cu}_{0.02}\text{Fe}_{0.2}\text{W}_{0.02}\text{TiO}_x$ catalyst (Fig. S14 in SI). As presented in Fig. S14 (A), the intensity of the adsorbed NH_3 species at 1736 , 1671 , 1598 , 1420 , 1264 , and 1216 cm^{-1} decreased gradually followed by switching to the $\text{NO} + \text{O}_2$ on $\text{Cu}_{0.02}\text{Fe}_{0.2}\text{W}_{0.02}\text{TiO}_x$. However, these peaks can still be observed at 5 min. For the NO_x reaction and the surface pre-adsorbed NH_3 without H_2O , the adsorbed NH_3 species vanished in 4 min (Fig. S14 (B)). Notably, H_2O influenced the reaction of NO_x and NH_3 over $\text{Cu}_{0.02}\text{Fe}_{0.2}\text{W}_{0.02}\text{TiO}_x$ to a certain extent although the NH_3 adsorption is unchanged under adding H_2O . This result can explain the decrease in NO conversion at low temperature in the presence of H_2O compared with that without H_2O . Combined with literature findings [58–60], water can inhibit the reaction between NO_x and the adsorbed ammonia, thus influencing the SCR activity.

In fact, according to the review by Lai and Wachs [58] and the related references [26,59–61], the effect of H_2O on the SCR activity is complex that can be proposed to two reasons: (1) competitive adsorption with NO or NH_3 and (2) inhibition of reaction between NO and the adsorbed NH_3 species. Based on our results, reason (2) is the prominent influence on the SCR activity than reason (1) over $\text{Cu}_{0.02}\text{Fe}_{0.2}\text{W}_{0.02}\text{TiO}_x$.

From another side, NH_3 and $\text{NO} + \text{O}_2$ species were introduced with the reverse order to investigate the reactivity of the adsorbed NO_x species over $\text{Cu}_{0.02}\text{Fe}_{0.2}\text{TiO}_x$ and $\text{Cu}_{0.02}\text{Fe}_{0.2}\text{W}_{0.02}\text{TiO}_x$ at 130°C . The *in situ* DRIFTS are displayed in Figs. 8(C and D). After $\text{NO} + \text{O}_2$ adsorption, the $\text{Cu}_{0.02}\text{Fe}_{0.2}\text{TiO}_x$ surface was covered with various N-containing species (1607 , 1582 , 1538 , 1288 , and 1247 cm^{-1}) (Fig. 8(C)). When the catalyst was exposed to NH_3 for 1 min, all the coordinated NH_3 (1603 , 1290 , and 1175 cm^{-1}) and cationic NH_4^+ species (1704 cm^{-1}) occurred immediately and bridging nitrates (1247 cm^{-1}) disappeared in 3 min. However, the bands attributed to the bridging monodentate nitrate/gas-phase NO_2 (1607 cm^{-1}) and chelating bidentate nitrates (1288 cm^{-1}) overlapping with coordinated NH_3 species (1290 and 1603 cm^{-1}) did not decrease with time. Specifically, the characteristic bands of the NO_x adsorbed species at 1582 and 1538 cm^{-1} exhibited a blue shift of the wavenumber after introducing NH_3 to the system. Increasing the temperature to 240°C (Fig. S15(A)), the bidentate nitrates (1351 cm^{-1}) and partial bridging nitrates species (1240 cm^{-1}) disappeared promptly with switching to NH_3 . The intensities of the bands attributed to most of the bridging monodentate nitrate (1602 cm^{-1}), monodentate nitrate species (1548 cm^{-1}), and all chelating bidentate nitrates (1581 cm^{-1}) gradually decreased. Those bands cannot be detected when injected with NH_3 for 20 min and covered by the NH_3 -adsorbed species. Ultimately, a blue shift of the band at 1548 and 1581 cm^{-1} also existed.

Nevertheless, as shown in Fig. 8(D), four types of absorption peaks were observed over the $\text{Cu}_{0.02}\text{Fe}_{0.2}\text{W}_{0.02}\text{TiO}_x$ surface after $\text{NO} + \text{O}_2$ pretreated: gaseous NO molecules (1895 cm^{-1}), bridging bidentate nitrates/gas-phase NO_2 (1624 cm^{-1}), bridging monodentate nitrates (1596 cm^{-1}), and chelating bidentate nitrates (1575 cm^{-1}). The bands corresponding to gaseous NO molecules were totally consumed immediately, whereas the bridging bidentate/monodentate nitrates and chelating bidentate nitrate species can still be observed after NH_3 adsorption, and all the coordinated NH_3 (1211 , 1273 , and 1596 cm^{-1}) and NH_4^+ species (1443 , 1672 , and 1739 cm^{-1}) can be detected in 1 min at 130°C . Meanwhile, the gaseous NO compounds (1897 cm^{-1}), bridging bidentate nitrates (1613 cm^{-1}), and bridging nitrate species (1239 cm^{-1}) disappeared rapidly in 1 min at 240°C (Fig. S15(B)). Interestingly, the depletion of nitrate species over $\text{Cu}_{0.02}\text{Fe}_{0.2}\text{W}_{0.02}\text{TiO}_x$ was faster than that over $\text{Cu}_{0.02}\text{Fe}_{0.2}\text{TiO}_x$. With prolonged time, only some adsorption NH_3 species, including NH_4^+ (1426 and 1726 cm^{-1}) and coordinated NH_3 species (1219 , 1265 and 1605 cm^{-1}), covered the

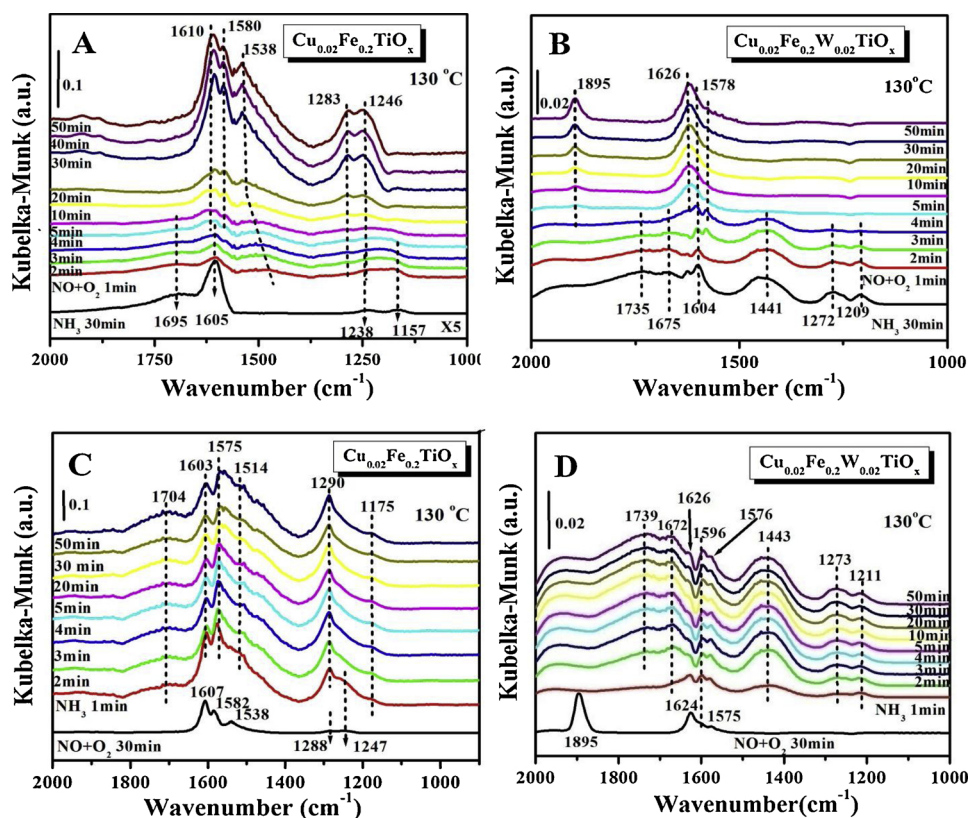


Fig. 8. *In-situ* DRIFTS of the reaction between NO_x and pre-adsorbed NH₃ on Cu_{0.02}Fe_{0.2}TiO_x (A) and Cu_{0.02}Fe_{0.2}W_{0.02}TiO_x (B) at 130 °C; the reaction between NH₃ and pre-adsorbed NO_x on Cu_{0.02}Fe_{0.2}TiO_x (C) and Cu_{0.02}Fe_{0.2}W_{0.02}TiO_x (D) at 130 °C. ([NO] = [NH₃] = 1000 ppm, [O₂] = 3 vol.%, N₂ as balance).

Cu_{0.02}Fe_{0.2}W_{0.02}TiO_x surface. Obviously, the adsorbed nitrate species was stable on both surfaces of Cu_{0.02}Fe_{0.2}TiO_x and Cu_{0.02}Fe_{0.2}W_{0.02}TiO_x at 130 °C, which may be activated and reacted with ammonia-derived species with increased temperature.

3.10. Kinetic study

Kinetic measurements are also conducted over the Cu_{0.02}Fe_{0.2}TiO_x and Cu_{0.02}Fe_{0.2}W_{0.02}TiO_x catalysts. According to literatures [58,62,63], the kinetics for the SCR reactions are often modeled using the following empirical kinetic equation in Eq. (3)

$$r_{\text{NO}} = k [\text{NO}]^{\alpha} [\text{NH}_3]^{\beta} [\text{O}_2]^{\gamma} \quad (3)$$

Where r_{NO} is the SCR rate, k is the apparent rate constant, and α , β , and γ represent the reaction orders for NO, NH₃, and O₂ respectively. Working in excess of oxygen, the O₂ concentration cannot substantially affect the resulting reaction rates and thus is allowed to be lumped in the reaction rate constants [54,58,62,64]. In kinetic measurements, only the reaction orders with respect to NO and NH₃ are explored over Cu_{0.02}Fe_{0.2}TiO_x and Cu_{0.02}Fe_{0.2}W_{0.02}TiO_x at different temperature. The results on the rate of NO conversion as a function of varying the inlet concentrations of NO/NH₃ in the range of 200–1000 ppm (another reactant NH₃/NO keeps at 500 ppm, O₂ is 3%) are depicted in Fig. 9. The reaction rate of NO increased with NO concentration over Cu_{0.02}Fe_{0.2}TiO_x and Cu_{0.02}Fe_{0.2}W_{0.02}TiO_x at various temperature (Fig. 9(A, B)). The reaction order α with respect to NO was calculated to be in range of 0.67 and 0.39 for Cu_{0.02}Fe_{0.2}TiO_x, and was far less than first order. It's worth noting that the reaction order for NO is low at 130 °C ($\alpha = 0.39$), indicating that NO involves in SCR reaction mainly as adsorbed species at low temperature, and the SCR reaction mainly follows the L-H mechanism. With increasing the reaction temperature, the value of α increased to 0.67, suggesting that the L-H mechanism no longer plays a dominant role in the reaction, and the E-R mechanism

may also occur in the SCR reaction. In other words, both E-R and L-H mechanisms may be coexistence in the SCR reaction at high temperature. These results are agreement with the literature reported [63].

For Cu_{0.02}Fe_{0.2}W_{0.02}TiO_x, the reaction order of NO (α) between 1.05 and 0.97 is close to first-order, which can explain that NO participates in SCR reaction in the form of gaseous or weakly adsorption, following mainly the E-R pathway [58,64]. This is consistence of the *in situ* DRIFTS results that the weak adsorption of NO_x is observed on the surface of Cu_{0.02}Fe_{0.2}W_{0.02}TiO_x.

While the reaction orders β for NH₃ is found to be close to zero for both Cu_{0.02}Fe_{0.2}TiO_x and Cu_{0.02}Fe_{0.2}W_{0.02}TiO_x catalysts (Fig. 9 (C, D)), suggesting that a strong adsorption of ammonia on the catalysts in the NH₃-SCR of NO reaction [63].

3.11. Combined effect of surface acidity and redox

Tungsten doping can efficiently promote the NH₃-SCR activity of the Cu_{0.02}Fe_{0.2}W_aTiO_x catalysts, especially under the feed gas stream containing 5 vol.% water. Meanwhile, the Cu_{0.02}Fe_{0.2}W_{0.02}TiO_x catalyst also reveals wide activity window (235–520 °C) with over 90% NO conversion and high sulfur/water resistance. According to the results of various characterizations, the tungsten addition tunes the surface species composition and surface acidity, enhancing the SCR activity.

Combined with the H₂-TPR results, the strong interactions among the copper, iron, and tungsten oxides exist in Cu_{0.02}Fe_{0.2}W_aTiO_x, influencing their reducibility derived from the tungsten addition by comparing with the H₂-TPR results of Fe_{0.2}W_{0.02}TiO_x, Cu_{0.02}W_{0.02}TiO_x, Cu_{0.02}Fe_{0.2}W_{0.02}TiO_x, Cu_{0.02}Fe_{0.2}TiO_x, Fe_{0.1}TiO_x, and Cu_{0.1}TiO_x. In the H₂-TPR curves (Fig. 4), the reduction temperature of all the peaks assigned to the reduction of the Fe oxides species shifts obviously toward the high value with increased W content. This phenomenon suggests that the reducibility of the Cu_{0.02}Fe_{0.2}W_aTiO_x catalysts is restrained compared with Cu_{0.02}Fe_{0.2}TiO_x catalyst.

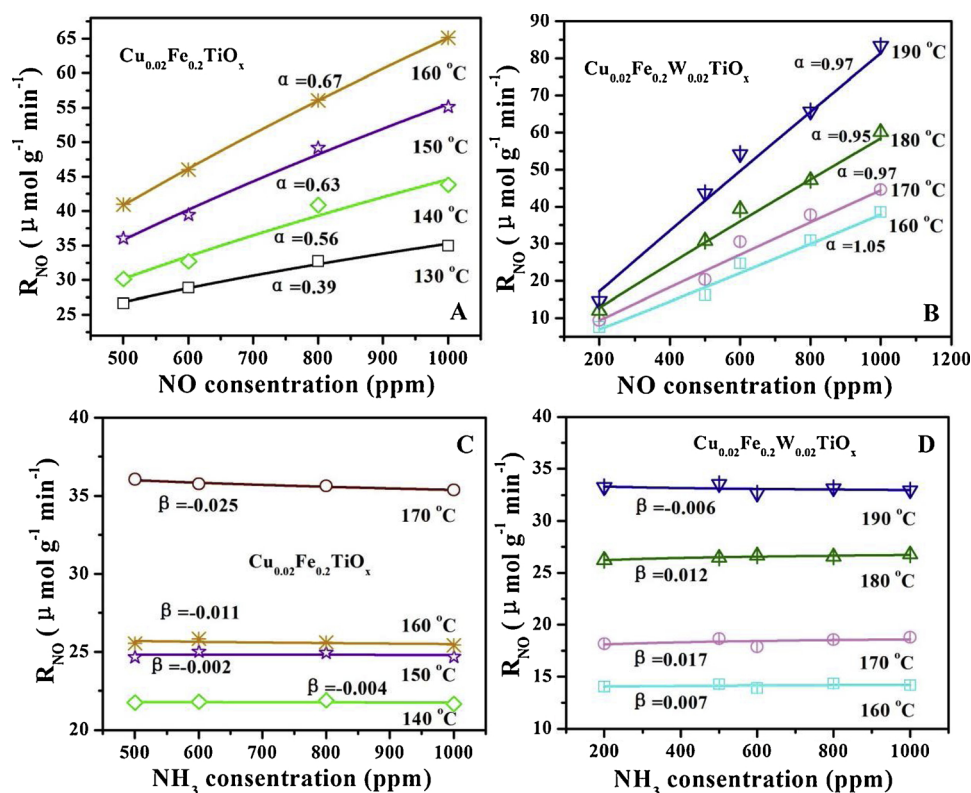


Fig. 9. Dependence of NO conversion rate on NO concentration over $\text{Cu}_{0.02}\text{Fe}_{0.2}\text{TiO}_x$ (A), $\text{Cu}_{0.02}\text{Fe}_{0.2}\text{W}_{0.02}\text{TiO}_x$ (B) and NH_3 concentration on $\text{Cu}_{0.02}\text{Fe}_{0.2}\text{TiO}_x$ (C), $\text{Cu}_{0.02}\text{Fe}_{0.2}\text{W}_{0.02}\text{TiO}_x$ (D) at different temperature. Reaction conditions: 35 mg catalyst, $[\text{NH}_3] = 500$ ppm, $[\text{NO}] = 200\text{--}1000$ ppm (A, B), $[\text{NO}] = 500$ ppm, $[\text{NH}_3] = 200\text{--}1000$ ppm (C, D), $[\text{O}_2] = 3\%$, N_2 balance, total flow 500 ml/min, GHSV = $1.0 \times 10^6 \text{ h}^{-1}$.

After introducing different amounts of tungsten, the effects of the tungsten addition on the surface species of the catalysts were investigated by XPS over $\text{Cu}_{0.02}\text{Fe}_{0.2}\text{W}_a\text{TiO}_x$ ($a = 0.01, 0.02, 0.03$). Given the no significant difference in the value of the surface $\text{Cu}^{2+}/(\text{Cu}^{2+} + \text{Cu}^+)$ ratio among $\text{Cu}_{0.02}\text{Fe}_{0.2}\text{W}_a\text{TiO}_x$ ($a = 0.01, 0.02, 0.03$) in Table 2, we believe that the tungsten addition has minimal influence on the surface copper species. In other words, the changes of the SCR activity with different W contents cannot be attributed to the amount of the surface Cu species. However, notably, the amount of iron species changes on the surface of the catalysts after tungsten addition. The XPS results show that the percentage of surface Fe^{3+} ($\text{Fe}_s^{3+}\%$) obviously decreases with increased tungsten content (Table 2), indicating that doping tungsten into $\text{Cu}_{0.02}\text{Fe}_{0.2}\text{TiO}_x$ restrains the redox ability of $\text{Cu}_{0.02}\text{Fe}_{0.2}\text{W}_a\text{TiO}_x$ consistent with the H_2 -TPR results. The $\text{Fe}_s^{3+}\%$ sequence is $\text{Cu}_{0.02}\text{Fe}_{0.2}\text{TiO}_x$ (6.53%) > $\text{Cu}_{0.02}\text{Fe}_{0.2}\text{W}_{0.01}\text{TiO}_x$ (3.92%) > $\text{Cu}_{0.02}\text{Fe}_{0.2}\text{W}_{0.02}\text{TiO}_x$ (3.66%) > $\text{Cu}_{0.02}\text{Fe}_{0.2}\text{W}_{0.03}\text{TiO}_x$ (2.02%). Moreover, as shown in Fig. S16 and Fig. 10, the contributions of Fe_s^{3+} and tungsten content to the NO conversion reveal that the NO conversion increased with doping Fe^{3+} (Fig. S16 in SI) and decreased with increased tungsten content at 130 and 160 °C (Fig. 10). The above results indicated that the difference in Fe_s^{3+} content was a major contributor to the change in NO conversion with different W amounts over $\text{Cu}_{0.02}\text{Fe}_{0.2}\text{W}_a\text{TiO}_x$. The redox circulation $\text{Fe}^{2+} \leftrightarrow \text{Fe}^{3+}$ reportedly contributes to NH_3 -SCR activity for iron-based catalysts [65]. The decrease in Fe_s^{3+} content can result in poor low-temperature NH_3 -SCR activity. Furthermore, the adsorbed NH_3 species is easily activated by Fe^{3+} to form $\text{Fe}^{2+} \cdot \text{NH}_2$ ($\text{Fe}^{3+} \cdot \text{NH}_3 + \text{O}^{2-} \rightarrow \text{Fe}^{2+} \cdot \text{NH}_2 + \text{OH}^-$) and then reacts with gaseous NO to form N_2 and H_2O ($\text{NH}_{3(\text{ad})} + \text{Fe}^{2+} \cdot \text{O} \cdot \text{NO} \rightarrow \text{Fe}^{2+} + \text{OH}^- + \text{N}_2 + \text{H}_2\text{O}$) [66]. In conclusion, tungsten addition probably has a great influence on the species of iron but not on the copper oxide species, thus affecting the catalytic activity of the $\text{Cu}_{0.02}\text{Fe}_{0.2}\text{W}_a\text{TiO}_x$ catalysts.

In addition, the acidity plays a key role in the NH_3 -SCR reaction [67]. Based on the NH_3 -TPD (Fig. 5) and *in situ* DRIFTS analysis (Fig. 7(A)), the tungsten addition can produce more acid sites, especially Brönsted acid sites, which effectively improve the adsorption and

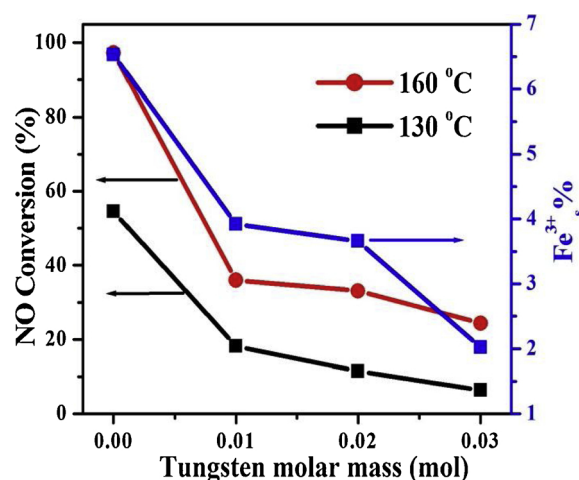


Fig. 10. Contributions of surface Fe_s^{3+} content and tungsten amount in $\text{Cu}_{0.02}\text{Fe}_{0.2}\text{W}_a\text{TiO}_x$ to the NO conversion at 130 and 160 °C in Fig. S3 (A).

activation of ammonia species and then promoting the SCR reaction. According to the results of DRIFTS in Section 3.9 and NH_3 -TPD, the NH_3 adsorption and activation capacity of $\text{Cu}_{0.02}\text{Fe}_{0.2}\text{W}_{0.02}\text{TiO}_x$ is apparently higher than that of $\text{Cu}_{0.02}\text{Fe}_{0.2}\text{TiO}_x$ and other $\text{Cu}_{0.02}\text{Fe}_{0.2}\text{W}_a\text{TiO}_x$ catalysts. Furthermore, Wang et al. proposed that the Brönsted acid sites may be conducive to the relatively low-temperature activity [68]. Meanwhile, the SCR reaction in the region of high temperature is likely controlled by the surface acidity [69]. The *in situ* DRIFTS results also confirm that the improved acidity due to the W addition can reduce the H_2O influence, enhancing the H_2O resistance over $\text{Cu}_{0.02}\text{Fe}_{0.2}\text{W}_{0.02}\text{TiO}_x$ compared with $\text{Cu}_{0.02}\text{Fe}_{0.2}\text{TiO}_x$.

In summary, although tungsten doping inhibits the redox property of the $\text{Cu}_{0.02}\text{Fe}_{0.2}\text{W}_{0.02}\text{TiO}_x$ catalyst, the acidity (mainly from Brönsted acidity) is enhanced due to the tungsten addition for $\text{Cu}_{0.02}\text{Fe}_{0.2}\text{W}_{0.02}\text{TiO}_x$. In general, the higher the redox property catalyst

has, the better low temperature SCR activity it exhibits [6–8,10,18]. Thereby, the $\text{Cu}_{0.02}\text{Fe}_{0.2}\text{TiO}_x$ catalyst displays good low temperature SCR activity due to its strong oxidation ability which is favor of the oxidation of NO to NO_2 , and the "fast SCR" reaction [70]. However, the low-temperature activity of $\text{Cu}_{0.02}\text{Fe}_{0.2}\text{W}_{0.02}\text{TiO}_x$ is only slightly lower than that of $\text{Cu}_{0.02}\text{Fe}_{0.2}\text{TiO}_x$. This fact can be attributed to the combined effects of its redox and high acidity of $\text{Cu}_{0.02}\text{Fe}_{0.2}\text{W}_{0.02}\text{TiO}_x$ although the redox property becomes weak after W addition compared with $\text{Cu}_{0.02}\text{Fe}_{0.2}\text{TiO}_x$. Moreover, high acidity can promote the SCR reaction in the region of high temperature. Thus, $\text{Cu}_{0.02}\text{Fe}_{0.2}\text{W}_{0.02}\text{TiO}_x$ exhibits the good SCR activity with wide activity window and N_2 selectivity. Interestingly, the $\text{Cu}_{0.02}\text{Fe}_{0.2}\text{W}_{0.02}\text{TiO}_x$ catalyst presents much better low-temperature SCR activity compared with other tungsten-modified catalysts reported in literatures (Table S2).

4. Conclusion

$\text{Cu}_{0.02}\text{Fe}_{0.2}\text{W}_a\text{TiO}_x$ oxides with a varied within the range of 0.01–0.03 were synthesized via one-pot sol–gel method. Among them, $\text{Cu}_{0.02}\text{Fe}_{0.2}\text{W}_{0.02}\text{TiO}_x$ catalyst shows the excellent NH_3 -SCR performance with a broad activity temperature window even in a rather high GHSV of $100,000\text{ h}^{-1}$ and compared with $\text{Cu}_{0.02}\text{Fe}_{0.2}\text{TiO}_x$ catalyst in the presence of 5 vol.% H_2O . Moreover, $\text{Cu}_{0.02}\text{Fe}_{0.2}\text{W}_{0.02}\text{TiO}_x$ catalyst exhibits a remarkable $\text{SO}_2 + \text{H}_2\text{O}$ resistance performance due to tungsten introduction. The influence of tungsten modification on the catalytic performance comes from the change of the surface acidity and surface species composition. The tungsten modification can facilitate the dispersion degree of the active species and increase the surface-chemisorbed labile oxygen and both Brönsted and Lewis acid sites (mainly of Brönsted acid sites) over the catalyst. The outstanding surface acidity and appropriate redox ability accelerate the adsorption and activation of ammonia, suggesting that the combined effects of redox and high acidity contribute the best NH_3 -SCR of NO activity over $\text{Cu}_{0.02}\text{Fe}_{0.2}\text{W}_{0.02}\text{TiO}_x$. The decrease in NO conversion at low temperature in the presence of H_2O compared with that without H_2O is ascribed to the inhibition of the reaction between NO_x and the adsorbed ammonia, thus influencing the SCR activity. Kinetic behavior of $\text{Cu}_{0.02}\text{Fe}_{0.2}\text{W}_{0.02}\text{TiO}_x$ is different from $\text{Cu}_{0.02}\text{Fe}_{0.2}\text{TiO}_x$ essentially, and the increased value of apparent activation energy with H_2O for $\text{Cu}_{0.02}\text{Fe}_{0.2}\text{W}_{0.02}\text{TiO}_x$ is less than that for $\text{Cu}_{0.02}\text{Fe}_{0.2}\text{TiO}_x$, suggesting the inhibition of water is slowed down by tungstate-doping. E–R reaction pathway is considered the dominant role from the *in situ* DRIFTS and kinetics results. This novel type catalyst can be a competitive catalyst in eliminating NO_x from stationary sources for the practical application.

Acknowledgements

This work is supported by Harbin science and technology innovation talent fund (Outstanding academic leader project) (RC2016XK015004), the Innovative Research Project of Key Laboratory of Functional Inorganic Material Chemistry (Heilongjiang University), Ministry of Education (2015).

Appendix A. Supplementary data

Supplementary material related to this article can be found, in the online version, at doi:<https://doi.org/10.1016/j.apcatb.2019.02.015>.

References

- [1] G. Yang, H.T. Zhao, X. Luo, K.Q. Shi, H.B. Zhao, W.K. Wang, Q.H. Chen, H. Fan, T. Wu, Appl. Catal. B: Environ. 245 (2019) 743.
- [2] Y. Xin, N.N. Zhang, Q. Li, Z.L. Zhang, X.M. Cao, L.R. Zheng, Y.W. Zeng, J.A. Anderson, Appl. Catal. B: Environ. 229 (2018) 81.
- [3] S. Gillot, G. Tricot, H. Vezin, J.P. Dacquin, C. Dujardin, P. Granger, Appl. Catal. B: Environ. 234 (2018) 318.
- [4] H. Liu, Z.X. Fan, C.Z. Sun, S.H. Yu, S. Feng, W. Chen, D.Z. Chen, C.J. Tang, F. Gao,

- Lin Dong, Appl. Catal. B: Environ. 244 (2019) 671.
- [5] M.H. Zhu, J.K. Lai, I.E. Wachs, Appl. Catal. B: Environ. 224 (2018) 836.
- [6] D.M. Meng, Q. Xu, Y.L. Jiao, Y. Guo, Y.L. Guo, L. Wang, G.Z. Lu, W.C. Zhan, Appl. Catal. B: Environ. 221 (2018) 652.
- [7] L.Q. Chen, R. Li, Z.B. Li, F.L. Yuan, X.Y. Niu, Y.J. Zhu, Catal. Sci. Technol. 7 (2017) 3243.
- [8] S.J. Yang, F.H. Qi, S.C. Xiong, H. Dang, Y. Liao, P.K. Wong, J.H. Li, Appl. Catal. B: Environ. 181 (2016) 570.
- [9] X.X. Wang, Q.L. Cong, L. Chen, Y. Shi, Y. Shi, S.J. Li, W. Li, Appl. Catal. B: Environ. 246 (2019) 166.
- [10] S. Ali, L.Q. Chen, Z.B. Li, T.R. Zhang, R. Li, S.U.H. Bakhtiar, X.S. Leng, F.L. Yuan, X.Y. Niu, Y.J. Zhu, Appl. Catal. B: Environ. 236 (2018) 25.
- [11] J. Han, J. Meeprasert, P. Maitarad, S. Nammuangruk, L.Y. Shi, D.S. Zhang, J. Phys. Chem. C 120 (2016) 1523.
- [12] Z.M. Liu, Y.X. Liu, B.H. Chen, T.L. Zhu, L.L. Ma, Catal. Sci. Technol. 6 (2016) 6688.
- [13] F.D. Liu, K. Asakura, H. He, Y.C. Liu, W.P. Shan, X.Y. Shi, C.B. Zhang, Catal. Today 164 (2011) 520.
- [14] F.D. Liu, H. He, J. Phys. Chem. C 114 (2010) 16929.
- [15] D. Wang, Y. Peng, S.C. Xiong, B. Li, L.N. Gan, C.M. Lu, J.J. Chen, Y.L. Ma, J.H. Li, Appl. Catal. B: Environ. 221 (2018) 556.
- [16] J. Liu, J. Meeprasert, S. Nammuangruk, K.W. Zha, H.R. Li, L. Huang, J. Phys. Chem. C 121 (2017) 4970.
- [17] L. Ma, J.H. Li, R. Ke, L.X. Fu, J. Phys. Chem. C 115 (2011) 7603.
- [18] Z.X. Ma, H.S. Yang, Q. Li, J.W. Zheng, X.B. Zhang, Appl. Catal. A Gen. 427–428 (2012) 43.
- [19] L. Zhu, Z.P. Zhong, H. Yang, C.H. Wang, J. Colloid Interface Sci. 478 (2016) 11.
- [20] Z.X. Ma, H.S. Yang, B. Li, F. Liu, X.B. Zhang, Ind. Eng. Chem. Res. 52 (2013) 3708.
- [21] S. Ali, L.Q. Chen, F.L. Yuan, R. Li, T.R. Zhang, S.U.H. Bakhtiar, X.S. Leng, X.Y. Niu, Y.J. Zhu, Appl. Catal. B: Environ. 210 (2017) 223.
- [22] Y. Peng, W.Z. Si, X. Li, J.M. Luo, J.H. Li, J. Crittenden, J.M. Hao, Appl. Catal. B: Environ. 181 (2016) 692.
- [23] P.G.W.A. Kompio, A. Brückner, F. Hipler, O. Manoylovad, G. Auer, G. Mestl, W. Grünert, Appl. Catal. B: Environ. 217 (2017) 365.
- [24] A. Suarez, A.S. Negreira, J. Wilcox, J. Phys. Chem. C 117 (2013) 24397.
- [25] K. Zhao, J.P. Meng, J.Y. Lu, Y. He, H.Z. Huang, Z.C. Tang, X.P. Zhen, Appl. Surf. Sci. 445 (2018) 454.
- [26] F.D. Liu, W.P. Shan, Z.H. Lian, J.J. Liu, H. He, Appl. Catal. B: Environ. 230 (2018) 165.
- [27] H. Wang, Z.P. Qu, S.C. Dong, H.B. Xie, C. Tang, Environ. Sci. Technol. 50 (2016) 13511.
- [28] W.P. Shan, F.D. Liu, H. He, X.Y. Shi, C.B. Zhang, Appl. Catal. B: Environ. 115–116 (2012) 100.
- [29] J. Liu, G.Q. Li, Y.F. Zhang, X.Q. Liu, Y. Wang, Y. Li, Appl. Surf. Sci. 401 (2017) 7.
- [30] Q.L. Chen, R.T. Guo, Q.S. Wang, W.G. Pan, W.H. Wang, N.Z. Yang, C.Z. Lu, S.X. Wang, Fuel 181 (2016) 852.
- [31] M. Kobayashi, K. Miyoshi, Appl. Catal. B: Environ. 72 (2007) 253.
- [32] Z.C. Si, D. Weng, X.D. Wu, J. Li, G. Li, J. Catal. 271 (2010) 43.
- [33] F.D. Liu, W.P. Shan, Z.H. Lian, L.J. Xie, W.W. Yang, H. He, Catal. Sci. Technol. 3 (2013) 2699.
- [34] Z.B. Xiong, J. Liu, F. Zhou, D.Y. Liu, W. Lu, J. Jin, S.F. Ding, Appl. Surf. Sci. 406 (2017) 218.
- [35] K. Routray, W. Zhou, C.J. Kiely, W. Grünert, I.E. Wachs, J. Catal. 275 (2010) 84.
- [36] P.R. Ettireddy, N. Ettireddy, T. Boningari, R. Pardemann, P.G. Smirniotis, J. Catal. 292 (2012) 53.
- [37] Y.V. Kolen'ko, K.A. Kovnir, A.I. Gavrilo, A.V. Garshev, P.E. Meskin, B.R. Churagulov, M. Bouchard, C.C. Justin, O.I. Lebedev, G.V. Tendeloo, M. Yoshimura, J. Phys. Chem. B 109 (2005) 20303.
- [38] X. Li, J.H. Li, Y. Peng, T. Zhang, S. Liu, J.M. Hao, Catal. Sci. Technol. 5 (2015) 4556.
- [39] X.J. Yao, L. Zhang, L.L. Li, L.C. Liu, Y. Cao, X. Dong, F. Gao, Y. Deng, C.J. Tang, Z. Chen, L. Dong, Y. Chen, Appl. Catal. B: Environ. 150–151 (2014) 315.
- [40] J. Engweiler, J. Harf, A. Baiker, J. Catal. 159 (1996) 259.
- [41] G. A'guila, F. Gracia, J. Corte's, P. Araya, Appl. Catal. B: Environ. 77 (2008) 325.
- [42] Z.H. Chen, F.R. Wang, H. Li, Q. Yang, L.F. Wang, X.H. Li, Ind. Eng. Chem. Res. 51 (2012) 202.
- [43] J.A. Horsley, I.E. Wachs, J.M. Brown, G.H. Via, F.D. Hardcastle, J. Phys. Chem. 91 (1987) 4014.
- [44] D.C. Vermaire, P.C.V. Berge, J. Catal. 116 (1989) 309.
- [45] V.M. Benitez, N.S. Figoli, Catal. Commun. 3 (2002) 487.
- [46] W.S. Hu, Y.H. Zhang, S.J. Liu, C.H. Zheng, X. Gao, I. Nova, E. Tronconi, Appl. Catal. B: Environ. 206 (2017) 449.
- [47] L.Y. Wang, X.X. Cheng, Z.Q. Wang, C.Y. Ma, Y.K. Qin, Appl. Catal. B: Environ. 201 (2017) 636.
- [48] C.C. Chusuei, M.A. Brookshier, D.W. Goodman, Langmuir 15 (1999) 2806.
- [49] Z. Wang, Z.Q. Qu, X. Quan, Z. Li, H. Wang, R. Fan, Appl. Catal. B: Environ. 134–135 (2013) 153.
- [50] L. Chen, J.H. Li, M.F. Ge, Environ. Sci. Technol. 44 (2010) 9590.
- [51] Z.B. Wu, B.Q. Jiang, Y. Liu, H.Q. Wang, R.B. Jin, Environ. Sci. Technol. 41 (2007) 5812.
- [52] G. Ramis, L. Yi, G. Busca, Catal. Today 28 (1996) 373.
- [53] N.Y. Topsoe, T. Slabick, B.S. Clausen, T.Z. Srnak, J.A. Dumesic, J. Catal. 134 (1992) 742.
- [54] M. Inomata, A. Miyamoto, Y. Murakami, J. Catal. 62 (1980) 140.
- [55] X.J. Yao, R.D. Zhao, L. Chen, J. Du, C.Y. Tao, F.M. Yang, L. Dong, Appl. Catal. B: Environ. 208 (2017) 82.
- [56] F.D. Liu, H. He, Y. Ding, C.B. Zhang, Appl. Catal. B: Environ. 93 (2009) 194.
- [57] X.J. Yao, Q. Yu, Z.Y. Ji, Y.Y. Lv, Y. Cao, C.G. Tang, F. Gao, L. Dong, Y. Chen, Appl.

- Catal. B: Environ. 130–131 (2013) 293.
- [58] J.K. Lai, I.E. Wachs, ACS Catal. 8 (2018) 6537.
- [59] I. Nova, L. Lietti, E. Tronconi, P. Forzatti, Chem. Eng. Sci. 56 (2001) 1229.
- [60] P. Forzatti, Catal. Today 62 (2000) 51.
- [61] J.A. Dumesic, N.Y. Topsøe, H. Topsøe, Y. Chen, T. Slabick, J. Catal. 163 (1996) 409.
- [62] R. Willi, M. Maciejewski, U. Göbel, R.A. Köppel, A. Baiker, J. Catal. 166 (1997) 356.
- [63] Z.R. Ma, X.D. Wu, H.N. Härelind, D. Weng, B.D. Wang, Z.C. Si, J. Mol. Catal. A: Chem. 423 (2016) 172.
- [64] G. Busca, L. Lietti, G. Ramis, F. Bertiv, Appl. Catal. B: Environ. 18 (1998) 1.
- [65] F.D. Liu, H. He, C.B. Zhang, Z.C. Feng, L.R. Zheng, Y.N. Xie, T.D. Hu, Appl. Catal. B: Environ. 96 (2010) 408.
- [66] C.X. Liu, S.J. Yang, L. Ma, Y. Peng, A. Hamidreza, H.Z. Chang, J.H. Li, Catal. Lett. 143 (2013) 697.
- [67] B. Liu, J. Liu, S.C. Ma, Z. Zhao, Y. Chen, X.Q. Gong, W.Y. Song, A.J. Duan, G.Y. Jiang, J. Phys. Chem. C 120 (2016) 2271.
- [68] X.X. Wang, Y. Shi, S.J. Li, W. Li, Appl. Catal. B: Environ. 220 (2018) 234.
- [69] L. Lietti, P. Forzatti, F. Bregani, Ind. Eng. Chem. Res. 35 (1996) 3884.
- [70] T. Sella, F. Gramigni, I. Nova, E. Tronconi, Appl. Catal. B: Environ. 225 (2018) 324.